EFFECT OF ANISOTROPY IN GROUND MOVEMENTS CAUSED BY TUNNELING

by

Despina M. Zymnis[1], Ioannis Chatzigiannelis[2], and Andrew J. Whittle[3]

ABSTRACT

This paper presents closed-form analytical solutions for estimating far-field ground deformations caused by shallow tunneling in a linear elastic soil mass with cross-anisotropic stiffness properties. The solutions describe 2-D ground deformations for uniform convergence (u_ε) and ovalization (u_δ) modes of a circular tunnel cavity, based on the complex formulation of planar elasticity and superposition of fundamental singularity solutions. The analyses are used to interpret measurements of ground deformations caused by open-face shield construction of a Jubilee Line Extension tunnel in London Clay at a well-instrumented site in St James Park. Anisotropic stiffness parameters are estimated from hollow cylinder tests on intact block samples of London Clay (from the Heathrow Airport Terminal 5 project) while the selection of the two input parameters is based on a least squares optimization using measurements of ground deformations. The results show consistent agreement with the measured distributions of surface and subsurface, vertical and horizontal displacement components, while anisotropic stiffness properties appear to have little effect on the pattern of ground movements. The results provide an interesting counterpoint to prior studies using FE analyses that have reported difficulties in predicting the distribution of ground movements for the instrumented section of the JLE tunnel.

[1] Ph.D Student, Massachusetts Institute of Technology, Cambridge MA
[2] Civil Engineer MSc, Dimitras 16A, Ag. Paraskevi, 15342, Greece
[3] Professor, Massachusetts Institute of Technology, Cambridge MA

INTRODUCTION

All tunnel operations cause movements in the surrounding soil. Figures 1a and 1b illustrate the primary sources of movements for cases of closed-face shield tunneling and open-face sequential support and excavation (often referred to as NATM), respectively. For open-face shield tunneling the stress changes around the tunnel face and the unsupported round length are primary sources of ground movements. Current geotechnical practice relies almost exclusively on empirical methods for estimating tunnel-induced ground deformations. Following Peck (1969) and Schmidt (1969) the transversal surface settlement trough can be fitted by a Gaussian function:

$$u_y\left(x,y\right)=u_y^0\exp\left(\frac{-x^2}{2x_i^2}\right) \tag{1}$$

where x is the horizontal distance from the tunnel centerline, u_y^0 the surface settlement at the tunnel centerline, and x_i, the location of the inflexion point.

Mair and Taylor (1997) show that the width of the settlement trough is well correlated to the depth of the tunnel, H, and to characteristics of the overlying soil (see Figure 2a). The same framework has been extended to subsurface vertical movements by varying the trough width parameter:

$$x_i=K\left(H-y\right) \tag{2}$$

where K is a non-linear function shown in Figure 2b.

There is very limited data for estimating the horizontal components of ground deformations. The most commonly used interpretation is to assume that the displacement vectors are directed to a point on or close to the center of the tunnel as proposed by Attewell (1978) and O'Reilly & New (1982) such that:

$$u_x \approx \left(\frac{x}{H}\right)u_y \tag{3}$$

There are also a variety of analytical solutions that have been proposed for estimating the 2-D distributions of ground movements for shallow tunnels. These analyses make simplifying assumptions regarding the constitutive behavior of soil and

ignore details of the tunnel construction procedure, but otherwise fulfill the principles of continuum mechanics. In principle, these analytical solutions provide a more consistent framework for interpreting horizontal and vertical components of ground deformations than conventional empirical models and use a small number of input parameters that can be readily calibrated to field data. They also provide a useful basis for evaluating the accuracy of numerical analyses.

The 'far-field' ground movements caused by shallow tunneling processes (excavation and support) are solved as a linear combination of deformation modes occurring at the tunnel cavity, Figure 3, with input parameters, u_ε and u_δ, corresponding to uniform convergence and ovalization, respectively. Pinto and Whittle (2011) have shown that closed-form solutions obtained by superposition of singularity solutions (after Sagaseta, 1987) provide a good approximation of the more complete ('Exact') solutions obtained by representing the finite dimensions of a shallow tunnel in a linear elastic soil (after Verruijt and Booker, 1996; Verruijt, 1997).

Pinto et al. (2011) have evaluated the analytical solutions through a series of case studies involving tunnels excavated through different ground conditions using a variety of closed and open-face construction methods. They generally found good agreement with measured data for tunnels constructed in low permeability clays assuming isotropic elastic properties. Although the analytical solutions do not model the actual tunnel construction process, selecting appropriate input parameters can very well capture the net effect of different construction methods. Pinto et al. (2011) noted significant limitations for the case of the Heathrow Express trial tunnel (Deane & Bassett, 1995) and the discrepancies between predicted and measured settlements were attributed to anisotropic stiffness properties of the heavily overconsolidated London Clay.

More recently Gasparre et al. (2007) have presented results from a comprehensive and definitive laboratory investigation of the stiffness properties of natural London Clay using block samples obtained during the excavations for Heathrow Terminal 5. Their test program included measurements of small strain elastic properties (based principally on wave propagation data using triaxial devices equipped with bender elements), limits on the reversible elastic response (referred to as the Y_1 yield condition) through drained and

undrained triaxial stress probe tests, and measurements of the degradation of secant stiffness parameters with strain level (using local strain measurements in triaxial and hollow cylinder devices). They conclude that the small strain behavior of the clay is well described by the framework of cross-anisotropic elasticity, and that 'significant anisotropy was revealed at all scales of deformation'.

This paper extends the analytical solutions presented by Pinto and Whittle (2011) to account for cross-anisotropic stiffness properties of the clay. The solutions are then evaluated through comparisons with data from the Jubilee Line Extension (JLE) project, involving open-face shield tunnel construction beneath a well-instrumented site in St James Park (Nyren, 1998). This is a very well instrumented and documented case site, with extensive supporting data on cross-anisotropic stiffness parameters for London clay reported by Gasparre et al. (2007). The JLE test section has been extensively analyzed by others using FE analyses and many have reported problems in predicting far-field deformations, and hence, provides an interesting opportunity to assess the capabilities of the proposed analytical solutions. Independent research by Puzrin et al (2012) has attempted to model the same case study using a related analytical approach.

ANALYTICAL SOLUTIONS FOR CROSS-ANISOTROPIC ELASTIC SOIL

The current analyses consider deformations in a vertical plane [x, y] through a cross-anisotropic, linear elastic soil with isotropic properties in a plane with dip angle α to the horizontal as shown in Figure 4. The stiffness parameters of the soil are given for a local [x', y', z'] coordinate system (Appendix A shows the transformation to the global frame [x, y, z]). The five independent anisotropic stiffness parameters are defined in the local coordinate system as E_1, the Young's modulus of the soil at a direction parallel to the isotropic plane, ν_1 the Poisson's ratio of strains in the isotropic plane (x'-z'), E_2, the Young's modulus normal to the isotropic plane, G_2, the shear modulus for strain in direction y', and ν_2, the Poisson's ratio for strain in y' direction due to strain in the x' direction.

Following Milne-Thompson (1960) and Lekhnitski (1977) the stress-strain relations for plane strain geometry conditions can be written as follows:

4

$$\begin{Bmatrix} \varepsilon_x \\ \varepsilon_y \\ \gamma_{xy} \end{Bmatrix} = \begin{bmatrix} \beta_{11} & \beta_{12} & \beta_{16} \\ \beta_{12} & \beta_{22} & \beta_{26} \\ \beta_{16} & \beta_{26} & \beta_{66} \end{bmatrix} \begin{Bmatrix} \sigma_x \\ \sigma_y \\ \tau_{xy} \end{Bmatrix} \tag{4a}$$

where the β_{ij} coefficients are related to the 5 independent stiffness parameters and the dip angle α as shown in Table 1. For $\alpha = 0°$ (i.e., isotropic properties in the horizontal plane), $E_1 = E_h$, $\nu_1 = \nu_{hh}$, $E_2 = E_v$, $\nu_2 = \nu_{vh}$, $G_2 = G_{vh}$ and the β_{ij} coefficients are:

$$\beta_{11} = \frac{1 - \nu_{hh}^2}{E_h}, \beta_{12} = -\frac{\nu_{vh}}{E_v}(1 + \nu_{hh}), \beta_{22} = \frac{1}{E_v}(1 - n\nu_{vh}^2), \beta_{66} = \frac{1}{G_{vh}}, \beta_{16} = \beta_{26} = 0 \tag{4b}$$

where the stiffness ratios $n = E_h/E_v$ and $m = G_{vh}/E_v$ are used later in the paper.

Figure 5 shows non-linear secant stiffness measurements of E_v, E_h and G_{vh} from drained hollow cylinder (HCA) uniaxial load tests on natural London Clay (unit B2) as functions of strain level (Gasparre et al., 2007). The data show that London Clay is strongly anisotropic at very small strain levels (true elastic range). The stiffness ratio, $n = E_h/E_v$, varies only slightly, $n = 1.72 - 2.30$, while $m = G_{vh}/E_v$ increases from 0.66 to 1.27 with increased strain level. The small strain stiffness ratios calculated from undrained tests are very similar to those from drained parameters as shown in Figure 5.

The elastic parameters are further constrained by thermodynamic considerations (e.g. Pickering 1970) such that:

$$G_{vh}, E_v, E_h > 0; \ 0 < n < 4; \ -1 < \nu_{hh} < 1; \ \nu_{hh} + 2 \nu_{hv} \nu_{vh} \le 1 \tag{4c}$$

The conditions for incompressibility are given by Gibson (1974) as:

$$\nu_{vh} = 0.5, \quad \nu_{hh} = 1 - 2n\nu_{vh}^2 = 1 - \frac{n}{2} \tag{4d}$$

In the absence of body forces, the stresses can be solved using the Airy Stress function, $F(x, y)$:

$$\beta_{22} \frac{\partial^4 F}{\partial x^4} - 2\beta_{26} \frac{\partial^4 F}{\partial x^3 \partial y} + (2\beta_{12} + \beta_{66}) \frac{\partial^4 F}{\partial x^2 \partial y^2} - 2\beta_{16} \frac{\partial^4 F}{\partial x \partial y^3} + \beta_{11} \frac{\partial^4 F}{\partial y^4} = 0 \tag{5}$$

5

with $\sigma_x = \dfrac{\partial^2 F}{\partial y^2}$; $\sigma_y = \dfrac{\partial^2 F}{\partial x^2}$; $\tau_{xy} = -\dfrac{\partial^2 F}{\partial x \partial y}$

Equation (5) is solved by means of the characteristic equation:

$$\beta_{11}\lambda^4 - 2\beta_{16}\lambda^3 + \left(2\beta_{12} + \beta_{66}\right)\lambda^2 - 2\beta_{26}\lambda + \beta_{22} = 0 \tag{6}$$

The roots of this equation are conjugate complex numbers, say $\lambda_1, \overline{\lambda}_1, \lambda_2, \overline{\lambda}_2$ and without loss of generality $\lambda_1 = a_1 + ib_1$, $\lambda_2 = a_2 + ib_2$, and $b_1 > b_2 > 0$. Any analytic function $g(x+\lambda y)$ satisfies eqn. (5) if λ is a solution to the characteristic equation. Since the resulting stress function must be real, the general solution is given by the following expression:

$$F(x,y) = 2\,\mathrm{Re}\left\{F_1(z_1) + F_2(z_2)\right\} = F_1(z_1) + \overline{F_1(z_1)} + F_2(z_2) + \overline{F_2(z_2)} \tag{7}$$

where $z_1 = x + \lambda_1 y$, $z_2 = x + \lambda_2 y$. Introducing the new functions: $\Phi_k(z_k) = F_k'(z_k)$, the stresses are found using the definition of complex variables z_1, z_2:

$$\sigma_x = 2\,\mathrm{Re}\left\{\lambda_1^2 \Phi_1'(z_1) + \lambda_2^2 \Phi_2'(z_2)\right\} \tag{8a}$$

$$\sigma_y = 2\,\mathrm{Re}\left\{\Phi_1'(z_1) + \Phi_2'(z_2)\right\} \tag{8b}$$

$$\tau_{xy} = -2\,\mathrm{Re}\left\{\lambda_1 \Phi_1'(z_1) + \lambda_2 \Phi_2'(z_2)\right\} \tag{8c}$$

and the displacements $U(x, y)$, $V(x, y)$ are found by integrating the strains:

$$U = 2\,\mathrm{Re}\left\{p_1 \Phi_1(z_1) + p_2 \Phi_2(z_2)\right\} \tag{9a}$$

$$V = 2\,\mathrm{Re}\left\{q_1 \Phi_1(z_1) + q_2 \Phi_2(z_2)\right\} \tag{9b}$$

where the coefficients p_k, q_k are expressed as:

$$p_k = \beta_{11}\lambda_k^2 + \beta_{12} - \beta_{16}\lambda_k; \quad q_k = \beta_{12}\lambda_k + \frac{\beta_{22}}{\lambda_k} - \beta_{26} \quad k = 1, 2 \tag{10}$$

Uniform Convergence Mode

For a cylindrical cavity of radius, R, in an infinite medium undergoing uniform convergence, u_ε, the displacement components at the tunnel wall can be expressed by (Figure 6a):

$$u_B(\theta) = u_\varepsilon \cos\theta = u_\varepsilon \left(\frac{e^{i\theta} + e^{-i\theta}}{2} \right) = u_\varepsilon \left(\frac{\sigma + \sigma^{-1}}{2} \right) \tag{11a}$$

$$v_B(\theta) = u_\varepsilon \sin\theta = u_\varepsilon \left(\frac{e^{i\theta} - e^{-i\theta}}{2i} \right) = u_\varepsilon \left(\frac{\sigma - \sigma^{-1}}{2i} \right) \tag{11b}$$

where $\sigma = e^{i\theta}$.

The circular boundary of the tunnel cavity in the [x, y] plane is transformed into an inclined ellipse in the plane of the complex variable $z = x + iy = Re^{i\theta} = R\sigma$ (Fig. 6b):

$$z_1 = x + \lambda_1 y = x + Re\{\lambda_1\} y + i\,Im\{\lambda_1\} y = x_1 + iy_1 \tag{12a}$$

$$z_2 = x + \lambda_2 y = x + Re\{\lambda_2\} y + i\,Im\{\lambda_2\} y = x_2 + iy_2 \tag{12b}$$

The boundary conditions can be solved by a further mapping onto a circle of unit radius as shown in Figure 6b:

$$z_k = R\left(\frac{1 - i\lambda_k}{2} \zeta_k + \frac{1 + i\lambda_k}{2} \frac{1}{\zeta_k} \right) \Leftrightarrow \zeta_k = \frac{z_k \pm \left[z_k^2 - R^2\left(1 + \lambda_k^2\right) \right]^{1/2}}{R(1 - i\lambda_k)} \tag{13}$$

$$k = 1, 2 \quad |\zeta_k| > 1$$

The analytic functions $\Phi_k(z_k)$ can be expressed as a Laurent series of the conformed variable ζ_k:

$$\Phi_1(z_1) = \Phi_1\big(z_1(\zeta_1)\big) = \Phi_1(\zeta_1) = \sum_{n=0}^{\infty} a_n \zeta_1^{-n} \tag{14a}$$

$$\Phi_2(z_2) = \Phi_2\big(z_2(\zeta_2)\big) = \Phi_2(\zeta_2) = \sum_{n=0}^{\infty} b_n \zeta_2^{-n} \tag{14b}$$

At the tunnel wall, $|z| = R$ and $\zeta_1 = \zeta_2 = e^{i\theta} = \sigma$. Hence, from Eqn. 9 the displacement components can be found from:

7

$$p_1 \sum_{n=0}^{\infty} a_n \sigma^{-n} + \overline{p}_1 \sum_{n=0}^{\infty} \overline{a}_n \sigma^n + p_2 \sum_{n=0}^{\infty} b_n \sigma^{-n} + \overline{p}_2 \sum_{n=0}^{\infty} \overline{b}_n \sigma^n = u_\varepsilon \frac{\sigma + \sigma^{-1}}{2} \tag{15a}$$

$$q_1 \sum_{n=0}^{\infty} a_n \sigma^{-n} + \overline{q}_1 \sum_{n=0}^{\infty} \overline{a}_n \sigma^n + q_2 \sum_{n=0}^{\infty} b_n \sigma^{-n} + \overline{q}_2 \sum_{n=0}^{\infty} \overline{b}_n \sigma^n = u_\varepsilon \frac{\sigma - \sigma^{-1}}{2i} \tag{15b}$$

Equating the coefficients for powers of σ:

$$n = 1: \begin{bmatrix} p_1 a_1 + p_2 b_1 = \dfrac{u_\varepsilon}{2} \\ q_1 a_1 + q_2 b_1 = \dfrac{iu_\varepsilon}{2} \end{bmatrix} \quad ; \quad n \neq 1: \begin{bmatrix} p_1 a_n + p_2 b_n = 0 \\ q_1 a_n + q_2 b_n = 0 \end{bmatrix} \tag{16}$$

The series coefficients are then solved as:

$$n = 1: \quad a_1 = \frac{u_\varepsilon}{2}\left(\frac{q_2 - ip_2}{p_1 q_2 - q_1 p_2} \right); \quad b_1 = \frac{u_\varepsilon}{2}\left(\frac{-q_1 + ip_1}{p_1 q_2 - q_1 p_2} \right) \tag{17}$$

$$n \neq 1: \quad a_n = b_n = 0$$

Ovalization Mode

The ovalization mode involves no ground loss and displacements at the tunnel cavity can be represented as follows:

$$u_B(\theta) = u_\delta \cos\theta = u_\delta \left(\frac{e^{i\theta} + e^{-i\theta}}{2} \right) = u_\delta \left(\frac{\sigma + \sigma^{-1}}{2} \right) \tag{18a}$$

$$v_B(\theta) = -u_\delta \sin\theta = -u_\delta \left(\frac{e^{i\theta} - e^{-i\theta}}{2i} \right) = -u_\delta \left(\frac{\sigma - \sigma^{-1}}{2i} \right) \tag{18b}$$

Applying the same methodology used above (for uniform convergence) the series coefficients a_n, b_n are found:

$$n = 1: \quad a_1 = \frac{u_\delta}{2}\left(\frac{q_2 + ip_2}{p_1 q_2 - q_1 p_2} \right); \quad b_1 = \frac{u_\delta}{2}\left(\frac{-q_1 - ip_1}{p_1 q_2 - q_1 p_2} \right) \tag{19}$$

$$n \neq 1: \quad a_n = b_n = 0$$

The displacements for uniform convergence and ovalization of a circular tunnel in an infinite cross-anisotropic elastic medium are then obtained by combining equations 17 or 19 with equations 14 and 9:

8

$$U(x,y) = 2\,\mathrm{Re}\left\{p_1 a_1 \frac{1}{\zeta_1(x,y)} + p_2 b_1 \frac{1}{\zeta_2(x,y)}\right\} \tag{20a}$$

$$V(x,y) = 2\,\mathrm{Re}\left\{q_1 a_1 \frac{1}{\zeta_1(x,y)} + q_2 b_1 \frac{1}{\zeta_2(x,y)}\right\} \tag{20b}$$

Effect of Traction-Free Ground Surface

Following Sagaseta (1987), the ground movements associated with a shallow tunnel, located at a depth H below the traction-free ground surface can be represented approximately through a singularity superposition technique, Figure 4. The deformation field for the shallow tunnel is represented by superimposing full-space solutions for a point source, [0, -H], and mirror image sink, [0, +H] (i.e., with equal and opposite cavity deformations) relative to the stress-free ground surface (y = 0), respectively:

Contracting tunnel ($-u_\varepsilon > 0$, $u_\delta > 0$):

$$u_x^+(x,y) = U_\varepsilon(x,y+H) + U_\delta(x,y+H)$$
$$u_y^+(x,y) = V_\varepsilon(x,y+H) + V_\delta(x,y+H) \tag{21}$$

Mirror image ($-u_\varepsilon < 0$, $u_\delta < 0$):

$$u_x^-(x,y) = U_\varepsilon(x,y-H) + U_\delta(x,y-H)$$
$$u_y^-(x,y) = V_\varepsilon(x,y-H) + V_\delta(x,y-H) \tag{22}$$

The resulting normal and shear tractions at the surface y = 0 due to these mirror images are as follows:

$$N^c(x) = \sigma_y^+(x,0) + \sigma_y^-(x,0) = \sigma_y(x,H) - \sigma_y(x,-H) = 0 \tag{23a}$$

$$T^c(x) = \tau_{xy}^+(x,0) + \tau_{xy}^-(x,0) = \tau_{xy}(x,H) - \tau_{xy}(x,-H) = -2\tau_{xy}(x,-H) \tag{23b}$$

A set of (equal and opposite) 'corrective' shear tractions $T^c(x)$ must then be applied at the free surface (Figure 4). The resulting displacements on a half-plane due to these corrective stresses are:

$$u_x^c = 2\,\mathrm{Re}\left\{p_1 \Phi_1^c(z_1) + p_2 \Phi_2^c(z_2)\right\}; \quad u_y^c = 2\,\mathrm{Re}\left\{q_1 \Phi_1^c(z_1) + q_2 \Phi_2^c(z_2)\right\} \tag{24}$$

where the analytic functions Φ_1^c, Φ_2^c are obtained through integration (after Lekhnitski, 1977):

9

$$\Phi_1^c(z_1) = \frac{1}{\lambda_1 - \lambda_2} \frac{1}{2\pi i} \int_{-\infty}^{\infty} \frac{\lambda_2 f_1(\xi) + f_2(\xi)}{\xi - z_1} d\xi \tag{25a}$$

$$\Phi_2^c(z_2) = -\frac{1}{\lambda_1 - \lambda_2} \frac{1}{2\pi i} \int_{-\infty}^{\infty} \frac{\lambda_1 f_1(\xi) + f_2(\xi)}{\xi - z_2} d\xi \tag{25b}$$

and the integrals of the normal and shear tractions along the boundary are:

$$f_1(s) = -\int_{\infty}^{s} N(x) dx = 0 \tag{25c}$$

$$f_2(s) = \int_{\infty}^{s} T(x) dx = \int_{\infty}^{s} T^c(x) dx \tag{25d}$$

Appendix B summarizes the solution of the infinite integrals in equations 25a, 25b, and 25d from which the following analytical functions are found:

$$\Phi_1^c(z_1) = \frac{2}{\lambda_1 - \lambda_2} \left[\lambda_1 \Phi_1(z_1 - \lambda_1 H) + \lambda_2 \Phi_2(z_1 - \lambda_2 H) \right] \tag{26a}$$

$$\Phi_2^c(z_2) = -\frac{2}{\lambda_1 - \lambda_2} \left[\lambda_1 \Phi_1(z_2 - \lambda_1 H) + \lambda_2 \Phi_2(z_2 - \lambda_2 H) \right] \tag{26b}$$

The final field of ground deformations for a shallow tunnel with uniform convergence at the tunnel cavity is then obtained from equations 21, 22 and 24:

$$u_x(x,y) = u_x^+(x,y) + u_x^-(x,y) + u_x^c(x,y) \tag{27a}$$

$$u_y(x,y) = u_y^+(x,y) + u_y^-(x,y) + u_y^c(x,y) \tag{27b}$$

Typical Results

Figures 7 and 8 illustrate the effects of cross-anisotropic stiffness properties on predictions of the shape of the surface settlement trough and lateral deflections for a 'reference inclinometer' offset at a distance $x/H = 1$ from the tunnel centerline. These results correspond to solutions for undrained deformations (i.e., incompressible conditions with Poisson's ratios defined in Eqn. 4d) for a shallow tunnel in clay with $R/H = 0.22$ (and typical cross-anisotropic stiffness ratios, n and m). Figure 7 shows that for horizontal planes of isotropy ($\alpha = 0°$), as the ovalization ratio $\rho = -u_\delta/u_\varepsilon$ increases the predicted settlement troughs become narrower and the surface centreline settlement u_y^0

10

increases significantly. For $\rho = 0$ the analyses predict inward horizontal displacements near the tunnel springline, while increases in ρ result in larger outward movements at this elevation (Fig. 7b). Figure 7 also illustrates results for cases where the plane of isotropy is dipping ($\alpha = 0°$, $15°$, $30°$, $45°$ and $\rho = 1$), representing (for example) conditions at the edge of a sedimentary basin. As the dip angle increases, the predicted surface centreline settlement u_y^0 increases, while the effect on the horizontal displacements is less pronounced.

Figure 8 shows the effects of the stiffness ratios, n and m for the case where the soil has isotropic properties in the horizontal plane ($\alpha = 0°$). The results show a narrowing of the surface settlement trough for normal stiffness ratios, $n > 1$ ($n = E_h/E_v = 1$ is isotropic case), which is especially pronounced for $n > 3$. Increases in the shear stiffness ratio, $m = G_{vh}/E_v$, have the opposite effect. The settlement trough for $m = 1$ is much wider than the isotropic case ($m = 0.33$). There is also a change in the mode shape of the settlement trough shown for $m = 1.5$, where the maximum settlement does not occur above the centerline, but is instead offset at $x/H \approx 0.5$. This result is often observed in 2-D finite element analyses of shallow tunnel excavation for cases with high in-situ K_0 stress conditions (e.g., Möller, 2006; Franzius et al., 2005; Addenbrooke et al., 1997), but has not been reported in prior tunneling projects. The transition in mode shape is a function of the anisotropic stiffness ratios (m and n) and the ovalization ratio, ρ, as shown in Figure 9. The subsequent applications of the analyses for the JLE tunnel use a constrained range of ρ to avoid the higher mode solutions.

PRIOR INTERPRETATION OF JLE TUNNEL IN ST JAMES PARK

The Jubilee Line Extension project (JLE, 1994-1999) included 15km of twin, 4.85m diameter, bored tunnels constructed using an open-face shield and excavated by mechanical backhoe. Ground displacements were measured at a well-instrumented greenfield site in St. James's Park and were described in detail by Nyren (1998). The Westbound (WB) tunnel passed under the instrumentation site in April 1995 with springline depth, H = 31m and an advance rate of 45.5m/day (i.e., 1.9m/hr). The EB tunnel (not considered in this paper) traversed the section in January 1996 at depth, H = 20.5m (and offset at 21.5m from the WB bore).

The instrumentation at the test section included an array of 24 Surface Monitoring Points (SMP; surveyed by total stations), while subsurface ground movements were recorded using a set of: 1) 9 electrolevel inclinometers, with tilt angles typically measured at vertical intervals of 2.5m; and 2) 11 rod extensometers, each measuring vertical displacement components at up to 8 elevations. Figure 10 shows eight locations (A-H) where 2D vectors of displacement can be interpreted from the inclinometer and extensometer data.

The soil profile comprises 12m of fill, alluvium and terrace gravels overlying a 40m thick unit of low permeability London Clay (with 4 divisions shown in Figure 10), above the Lambeth Group (lower aquifer system). The groundwater table is located approximately 3m below ground surface but pore pressures are 5 - 7m below hydrostatic at the elevation of the WB tunnel springline. Standing and Burland (2006) have carried out a detailed review of the physical and engineering properties of the four divisions of the London Clay along this section of the JLE alignment. They report the undrained shear strength of London Clay increasing from, $s_u = 215\pm80$kPa (unit A3) to 233 ± 77kPa (A2), and in-situ hydraulic conductivity values, $k = 0.15 - 2.0 \times 10^{-10}$ m/s.

Surface Displacements

Figures 11a and 11b show the vertical and horizontal surface movements measured approximately 1 day after the passage of the WB tunnel face, when it can reasonably be assumed that there is little consolidation within the London clay. Standing and Burland (2006) fitted the transversal surface settlement trough using the empirical Gaussian relation (eqn. 1) with a trough width, $x_i = 13.3$m (i.e., $K = x_i/H = 0.43$) and maximum settlement above the crown, $u_y^0 \approx 20$mm. Hence, the volume loss at the ground surface, ΔV_s ($=2.5u_y^0 x_i$) corresponds to an apparent ground loss at the tunnel cavity, $\Delta V_L/V_0 = 3.3\%$, caused by tunnel construction. They attribute this unexpectedly high volume loss to details of the construction method (the WB tunnel was constructed with up to 1.9m of unsupported heading) and to a local ground zone above the WB tunnel crown with a higher concentration of sand and silt partings in the London Clay.

The horizontal surface displacements (Fig. 9b) are also well fitted by conventional empirical assumptions using eqn. 3 with maximum surface horizontal movement $u_x \approx$

5.7mm at x ≈ 14m east of the centreline. However, it should be noted that the measured profile shows a loss of anti-symmetry (e.g., $u_x \neq$ 0mm at x = 0m) that Nyren (1998) attributes to a deviation in principal stresses acting in the horizontal plane.

Prior Numerical Analyses

Franzius et al (2005) used non-linear finite element analyses to evaluate the measured ground movements reported by Nyren (1998). They compare 2D and 3D analyses, using different coefficients of lateral earth pressure at rest, K_0 and various constitutive models for simulating the construction of the JLE WB tunnel. Their base case scenario used a non-linear, isotropic elasto-plastic constitutive model with $K_0 = 1.5$. For an assumed volume loss, $\Delta V_L/V_0 = 3.3\%$, this resulted in a computed maximum surface settlement $u_y^0 = 10$mm and a transverse surface settlement trough that was much wider than the measured behavior, Figure 12. Similar results were obtained using 3D analyses with more refined modeling of the tunnel heading.

The Authors modified the constitutive model to include non-linear cross-anisotropic stiffness properties (using a simplified 3 parameter formulation proposed by Graham and Houlsby, 1983). They were only able to achieve good agreement with the measured settlement trough in the 2D analyses using an unrealistically high elastic Young's modulus ratio, $n = E_h/E_v = 6.5$ (i.e., outside the theoretical elastic range of n, eqn. 4b) in combination with a low value of $K_0 = 0.5$. However, when the same model parameters were used in a 3D analysis of the open-face tunnel construction, much larger surface settlements were obtained ($u_y^0 = 85$mm with interpreted volume loss, $\Delta V_L/V_0 = 18\%$) as shown in Figure 12.

Wongsaroj (2005) formulated a bespoke constitutive model to describe the non-linear, anisotropic behavior of London clay and used the model in 3D finite element simulations for short and long-term ground movements caused by JLE tunnel construction. Figure 13 compares the measured surface settlements with computed results using four different input parameter sets. Models with both isotropic and anisotropic small strain stiffness ($K_0 = 1.5$; small strain, drained elastic stiffness ratios, n = 0.44, m = 0.13, that are inconsistent with data shown in Fig. 5) resulted in settlement troughs that are wider than the field measurements for the WB JLE tunnel and also

13

overestimate significantly the back-figured volume loss ($\Delta V_L/V_0$ = 5.4% to 6.0%). Good agreement is only achieved by increasing the anisotropic stiffness ratio (G_{hh}/G_{vh} = 5 corresponding to m = 0.04) and reducing the assumed value of K_0 = 1.2. Figure 13b shows further comparisons with the subsurface horizontal displacements reported by Wongsaroj (2005). The analyses generally predict larger lateral deformations of the soil towards the tunnel centerline than are measured in the field. The Author attributed this discrepancy, in part, to surveying errors in the field measurements. Subsurface horizontal displacements were not reported for the fourth model (G_{hh}/G_{vh} = 5) and thus are not shown in Figure 13b.

APPLICATION OF ANALYTICAL SOLUTIONS

The input parameters for the analytical solutions are interpreted from the measured ground deformations of the WB JLE tunnel in St James Park through a least squares fitting approach. The analyses assume linear elastic behavior throughout the soil mass and hence, are likely to underestimate ground deformations close to the tunnel lining where plastic failure occurs in the clay.

This near-field zone of plasticity can be estimated from solutions of a cylindrical cavity contraction in an elastic-perfectly plastic soil (e.g., Yu and Rowe, 1999). The radius of the plastic zone, R_p can be found from:

$$\frac{R_p}{R} = \exp\left(\frac{N-1}{2}\right) \tag{28}$$

where $N = (p_0 - p_i)/s_u$ is the overload factor, p_0 and p_i are the pressures in the far field and within the tunnel cavity.

The radius of the plastic zone can then be estimated by 1) equating p_0 with the overburden pressure ($\sigma_{v0} \approx$ 600kPa) at the springline, 2) assuming p_i = 0; and 3) considering a likely range of undrained shear strength for the London Clay, s_u = 136 − 293 kPa (A3 unit; Standing & Burland, 2006). Based on these assumptions, $R_p \approx$ 4 - 13m. The current interpretation excludes measured data within the estimated plastic zone but considers 46 of subsurface deformations (along 8 vertical lines, A-H, Fig. 5) together with 24 locations where surface movements were surveyed. Figure 14 shows the derivation of the least squares solution error (LSS) for the input parameter state space (u_ε,

14

u_δ), where:

$$LSS = Min \sum_i \left\{ \left(\tilde{u}_{xi} - u_{xi}\right)^2 + \left(\tilde{u}_{yi} - u_{yi}\right)^2 \right\} \qquad (29)$$

In most practical cases, engineers will expect to fit the measured centerline surface settlement, u_y^0, and hence, it is preferable to present a modified least squares solution, LSS*, that includes this additional constraint.

Figures 14a and 14b compare results for two sets of soil stiffness properties a) isotropic case (m = 0.33, n = 1, $\nu = \nu_{vh} = \nu_{hh} = 0.5$); and b) cross-anisotropic case (with α = 0°), based on the small strain behavior reported by Gasparre et al (2007) and assuming incompressibility of the London clay (m = 0.66, n = 2.07, $\nu_{vh} = 0.5$, $\nu_{hh} = [1 - 0.5n] = -0.035$). It should be noted that the small strain elastic anisotropic stiffness ratio n = E_h/E_v obtained from undrained tests is very close to that obtained from drained tests as shown in Gasparre et al (2007).

There is little difference in the magnitude of the global least squares error between the two sets of analyses, while the constrained LSS* solution for the isotropic case is slightly closer to the global minimum than the cross-anisotropic case. The derived cavity contraction parameter is smaller for the cross-anisotropic case (-u_ε = 34mm vs 36mm for the isotropic case), with a lower relative distortion, $\rho = -u_\delta/u_\varepsilon$ = 1.56 vs 1.32). Both LSS* solutions imply slightly lower volume loss ratios at the tunnel cavity ($\Delta V_L/V_0$ = 3.0% and 2.8%; Figs. 14a, 14b, respectively) than were estimated by conventional empirical solutions (3.3%; Fig. 11a).

Figure 15 compares analytical solutions of the distributions of vertical and horizontal surface displacement components for the WB JLE tunnel, using isotropic and cross-anisotropic soil properties (with LSS* tunnel mode input parameters). The fields of vertical displacements are very similar for both sets of analyses, while the cross-anisotropic case predicts slightly larger lateral ground movements around the tunnel springline than the isotropic case (Fig. 15b).

Figures 16a and 16b show that both sets of analysis produce very reasonable agreement with the measured vertical and horizontal surface displacements. These results show that reasonable predictions of surface displacements can be achieved using the analytical solutions with isotropic stiffness properties for the London Clay. This is a

15

very surprising result that is due to counteracting effects of the two key stiffness ratios, n and m (cf. Figs. 8a, 8b).

Figures 17a and 17b compare the computed and measured subsurface vertical and horizontal displacement components for the WB JLE tunnel. The computed deformations are generally in very good agreement with both vertical and horizontal components of movements measured in the far field (i.e., outside the expected zone of plastic soil behavior). Very similar patterns of soil displacements are obtained using isotropic and anisotropic elastic stiffness parameters. The analysis tends to overestimate measured centerline vertical settlements below 10m but produce very accurate predictions at the rest of the extensometer positions. The analytical solutions fit well the inclinometer readings at locations from the ground surface up to a transition depth marked by contour line $u_x = 0$mm in Figure 17b, but predict outward movement below this transition depth while the inclinometers show zero ground movements.

CONCLUSIONS

This paper has presented new analytical solutions for estimating 2D ground deformations caused by shallow tunneling in a cross-anisotropic soil. These analyses extend prior solutions derived by Pinto (1999), Whittle and Sagaseta (2003) and Pinto and Whittle (2011) in which the complete distribution of far-field ground movements can be interpreted from two basic tunnel cavity deformation mode parameters (u_ε and u_δ or ρ), the dip angle of the isotopic stiffness plane, α, and two key anisotropic stiffness ratios, n $= E_h/E_v$ and m $= G_{vh}/E_v$.

The analytical solutions have been applied to re-interpret ground deformations associated with the open-face construction of the WB tunnel for the Jubilee Line at a well-instrumented site in St. James Park (Nyren, 1998). The current analyses benefit from high quality measurements of the cross-anisotropic stiffness properties of intact London Clay measured in an independent study for Heathrow Airport T5 (Gasparre et al., 2007). These data show that London Clay exhibits pronounced stiffness anisotropy at small strain levels.

The cavity deformation mode parameters are evaluated using a least squares fit to surface and subsurface deformations at the instrumented test site. The results show that

16

both the isotropic and cross-anisotropic analytical solutions produce very good fits to the measured ground displacements. Using the high quality measurements undertaken by Gasparre et al (2007), it can indeed be concluded that cross-anisotropic stiffness parameters have only a small influence on predictions of the far-field ground deformations caused by tunneling in London Clay. The analytical solutions achieve comparable levels of agreement with measurements of the surface settlement trough that are conventionally fitted using an empirical Gaussian distribution function. However, the current analytical solutions correspond to smaller volume losses at the tunnel cavity than those estimated by conventional empirical assumptions (cf., Standing & Burland, 2006) while offering a more consistent framework for interpreting the complete distribution of horizontal and vertical components of ground deformations. Although these results are very encouraging, further case studies are needed to establish how the cavity mode parameters are related to different methods of tunnel construction.

17

REFERENCES

Addenbrooke, T. I., Potts, D. M. & Puzrin, A. M. (1997); "The influence of pre-failure soil stiffness on the numerical analysis of tunnel construction," *Géotechnique,* 47(3), 693-712.

Attewell, P.B. (1978); "Ground movements caused by tunnelling in soil," *Proc. Int. Conf. on Large movements and Structures (ed. J. D. Geddes),* Pentech Press, London, 812-948.

Deane, A. P., and Bassett, R. H. (1995); "The Heathrow Express Trial Tunnel". *Proc. Instn. of Civ. Engrs, Geotech. Engng.*, 113, 144-156.

Franzius, J.N., Potts, D.M. and Burland, J.B. (2005), "The influence of soil anisotropy and K_0 on ground movements resulting from tunnel excavation," *Géotechnique,* 55(3), 189-199.

Gasparre, A., Nishimura, S., Minh, N.A., Coop, M.R. and Jardine, R.J. (2007); "The stiffness of natural London Clay," *Géotechnique,* 57(1), 33-47.

Gibson, R. E. (1974); "The analytical method in soil mechanics," *Géotechnique,* 24(2), 115-140.

Graham, J. and Houlsby, G.T. (1983); "Anisotropic elasticity of a natural clay," *Géotechnique,* 33(2), 165-180.

Lekhnitskii, S.G. (1963); "Theory of Elasticity of an anisotropic elastic body," Holden-Day, San Francisco

Mair, R.J., and Taylor, R.N. (1997); "Bored Tunneling in the Urban Environment," *Proceedings of the 14th International Conference on Soil Mechanics and Foundation Engineering,* Hamburg, pp. 2353–2385.

Milne-Thompson, L.M. (1960); "*Plane Elastic Systems*," Berlin, Springer-Verlag

Möller, S. (2006); "Tunnel induced settlement and structural forces in linings," Ph.D. Thesis, Institut für Geotechnik, Universität Stuttgart

Nyren, R.J. (1998); "Field measurements above twin tunnels in London Clay," *PhD thesis*, Imperial College, University of London.

O'Reilly, M.P., and New, B.M. (1982); "Settlements above tunnels in United Kingdom—their magnitude and prediction," *Tunnelling 82*, London, IMM, 173–181.

Peck, R.B. (1969); "Deep Excavations and Tunnels in Soft Ground," *Proceedings of the 7th International Conference on Soil Mechanics and Foundation Engineering*, Mexico City, State of the Art Volume, pp. 225-290.

Pinto, F. (1999); "Analytical methods to interpret ground deformations due to soft ground tunneling," SM Thesis, MIT Department of Civil & Environmental Engineering, Cambridge, MA.

Pinto, F. and Whittle, A.J. (2011); "Ground Movements due to shallow tunnels in soft ground: 1. Analytical solutions," *Accepted for publication ASCE Journal of Geotechnical and Geoenvironmental Engineering*.

Pinto, F., Zymnis D.M., and Whittle, A.J. (2011); "Ground Movements due to shallow tunnels in soft ground: 2. Analytical interpretation and prediction," *Accepted for publication ASCE Journal of Geotechnical and Geoenvironmental Engineering*.

Puzrin, A.M., Burland J.B., and Standing, J.R. (2012); "Simple approach to predicting ground displacements caused by tunnelling in undrained anisotropic elastic soil," *Géotechnique,* 62(4), 341–352.

Sagaseta, C. (1987); "Analysis of undrained soil deformation due to ground loss," *Géotechnique* 37(3), 301-320.

Schmidt, B. (1969); "Settlements and ground movements associated with tunneling in soils," *PhD Thesis*, University of Illinois, Urbana.

Standing, J.R. and Burland, J.B. (2006); "Unexpected tunnelling volume losses in the Westminster area, London," *Géotechnique,* 56(1), 11-26.

Verruijt, A. (1997); "A complex variable solution for a deforming tunnel in an elastic half-plane," *International Journal for Numerical and Analytical Methods in Geomechanics*, 21, 77-89.

Verruijt, A. & Booker, J. R. (1996); "Surface settlements due to deformation of a tunnel in an elastic half-plane," *Géotechnique*, 46(4), 753-756.

Whittle A.J., & Sagaseta, C. (2003); "Analyzing the effects of gaining and losing ground," *Soil Behavior and Soft Ground Construction*, ASCE GSP No. 119, 255-291.

Wongsaroj, J. (2005); "Three-dimensional finite element analysis of short and long-term ground response to open-face tunneling in stiff clay," *PhD thesis*, University of Cambridge.

Yu, H.S. & Rowe, R.K. (1999); " Plasticity solutions for soil behavior around contracting cavities and tunnels," *International Journal for Numerical and Analytical Methods in Geomechanics*, 23(12), 1245-1279.

APPENDIX A

Rotation of Planes from Local to Global Coordinate System

Considering a cross-anisotropic, linear elastic soil with isotropic properties in a general $[x', z']$ plane with dip angle α to the horizontal as shown in Figure 4, the strains are related to the stresses in the local $[x', y', z']$ coordinate system through the following relation:

$$
\begin{Bmatrix} \varepsilon_{x'x'} \\ \varepsilon_{y'y'} \\ \varepsilon_{z'z'} \\ \gamma_{x'y'} \\ \gamma_{x'z'} \\ \gamma_{y'z'} \end{Bmatrix} =
\begin{bmatrix}
\dfrac{1}{E_1} & -\dfrac{\nu_2}{E_2} & -\dfrac{\nu_1}{E_1} & 0 & 0 & 0 \\[2mm]
-\dfrac{\nu_2}{E_2} & \dfrac{1}{E_2} & -\dfrac{\nu_2}{E_2} & 0 & 0 & 0 \\[2mm]
-\dfrac{\nu_1}{E_1} & -\dfrac{\nu_2}{E_2} & \dfrac{1}{E_1} & 0 & 0 & 0 \\[2mm]
0 & 0 & 0 & \dfrac{1}{G_2} & 0 & 0 \\[2mm]
0 & 0 & 0 & 0 & \dfrac{2(1+\nu_1)}{E_1} & 0 \\[2mm]
0 & 0 & 0 & 0 & 0 & \dfrac{1}{G_2}
\end{bmatrix}
\begin{Bmatrix} \sigma_{x'x'} \\ \sigma_{y'y'} \\ \sigma_{z'z'} \\ \sigma_{x'y'} \\ \sigma_{x'z'} \\ \sigma_{y'z'} \end{Bmatrix} = C_{x'y'z'}\sigma_{x'y'z'} \quad (A1)
$$

The local material compliance matrix $C_{x'y'z'}$ is transformed to the global compliance matrix C_{xyz} as shown below:

$$
\varepsilon_{xyz} = C_{xyz}\sigma_{xyz} = R^T C_{x'y'z'} R \sigma_{xyz}
$$

$$(A2)$$

where R is the transformation matrix:

$$
R = \begin{bmatrix}
\cos^2\alpha & \sin^2\alpha & 0 & 0 & 0 & -\sin 2\alpha \\
\sin^2\alpha & \cos^2\alpha & 0 & 0 & 0 & \sin 2\alpha \\
0 & 0 & 1 & 0 & 0 & 0 \\
0 & 0 & 0 & \cos\alpha & \sin\alpha & 0 \\
0 & 0 & 0 & -\sin\alpha & \cos\alpha & 0 \\
0.5\sin 2\alpha & -0.5\sin 2\alpha & 0 & 0 & 0 & \cos 2\alpha
\end{bmatrix} \quad (A3)
$$

21

APPENDIX B

Calculation of corrective stresses integrals

The integral of the tractions along the free surface (eq. 22d) after some manipulation reduces to:

$$f_2(s) = 2\left\{\lambda_1\Phi_1(s-\lambda_1 H) + \overline{\lambda_1\Phi_1(s-\lambda_1 H)} + \lambda_2\Phi_2(s-\lambda_2 H) + \overline{\lambda_2\Phi_2(s-\lambda_2 H)}\right\}, s \in \mathbb{R} \quad \text{(B1)}$$

The calculation of the stress functions of the corrective stresses $F_1^c(z_1)$, $F_2^c(z_2)$ requires the calculation of the infinite integral (eq. 25a):

$$
\begin{aligned}
\Phi_1^c(z_1) &= \frac{1}{\lambda_1-\lambda_2}\frac{1}{2\pi i}\int_{-\infty}^{\infty}\frac{\lambda_2 f_1(\xi)+f_2(\xi)}{\xi-z_1}d\xi = \frac{1}{\lambda_1-\lambda_2}\frac{1}{2\pi i}\int_{-\infty}^{\infty}\frac{f_2(\xi)}{\xi-z_1}d\xi \\
&= \frac{1}{\lambda_1-\lambda_2}\frac{1}{\pi i}\sum_{k=1}^{2}\left\{\int_{-\infty}^{\infty}\frac{\lambda_k\Phi_k(\xi-\lambda_k H)}{\xi-z_1}d\xi + \int_{-\infty}^{\infty}\frac{\overline{\lambda_k\Phi_k(\xi-\lambda_k H)}}{\xi-z_1}d\xi\right\}
\end{aligned} \quad \text{(B2)}
$$

Consider the integrals of the complex functions $\dfrac{\Phi_k(w)}{w-z}, \dfrac{\overline{\Phi_k(w)}}{w-z}$ along the path shown in Figure B1. This path includes branch points for function F_k

$$w_{1,2} = \lambda_k H \pm R\sqrt{1+\lambda_k^2} \quad \text{(B3)}$$

For small ratios R/H, and usual degrees of anisotropy function the two branch points of the F_k will lie in the upper plane (i.e., outside the chosen integration path) and therefore the integral of the analytic function F_k according to the Cauchy integral formula assumes the value:

$$\oint_c \frac{\Phi_k(w)}{w-z}dw = 2\pi i\Phi_k(z), \quad \oint_c \frac{\overline{\Phi_k(w)}}{w-z}dw = 0 \quad \text{(B4)}$$

Also: $\oint_c \dfrac{\Phi_k(w)}{w-z}dw = \lim_{R\to\infty}\left[\int_R^{-R}\frac{\Phi_k(\xi)}{\xi-z}d\xi + \int_{I_R}\frac{\Phi_k(w)}{w-z}dw\right] = -\int_{-\infty}^{\infty}\frac{\Phi_k(\xi)}{\xi-z}d\xi \quad \text{(B5)}$

The final result is $\Phi_1^c(z_1) = \dfrac{2}{\lambda_1-\lambda_2}\left[\lambda_1\Phi_1(z_1-\lambda_1 H)+\lambda_2\Phi_2(z_1-\lambda_2 H)\right]$ \quad (B6a)

Similarly, $\Phi_2^c(z_2) = -\dfrac{2}{\lambda_1-\lambda_2}\left[\lambda_1\Phi_1(z_2-\lambda_1 H)+\lambda_2\Phi_2(z_2-\lambda_2 H)\right]$ \quad (B6b)

LIST OF SYMBOLS

<u>Latin</u>

a_n Laurent series coefficients

b_n Laurent series coefficients

C integration path

E_1 Young's modulus at the direction parallel to the isotropic plane

E_2 Young's modulus at the direction normal to the isotropic plane

E_h Young's modulus in (any) horizontal direction (plane of isotropy)

E_v Young's modulus in the vertical direction

$f_k(x)$ integral of traction along boundary

F   Airy's stress function

G_2 Shear modulus for strain in direction normal to the isotropic plane

G_{hh} shear modulus for strain in the horizontal plane

G_{vh} shear modulus for strain in (any) vertical plane (planes of anisotropy)

H depth to tunnel springline

i imaginary unit

k hydraulic conductivity

K empirical parameter related to the settlement trough width

K_0 coefficient of lateral earth pressure at rest

L radius of integration path

LSS least squares solution

LSS^* constrained least squares solution that fits u_y^0

n, m stiffness ratios

$N(x)$ normal traction on free surface

N overload factor

p_k, q_k analytic coefficients

p_0 pressure outside the tunnel cavity

p_i pressure inside the tunnel cavity

R radius of tunnel

R_p radius of plastic zone

s variable

S_k boundary in z_k domain

s_u undrained shear strength

$T(x)$ shear traction on free surface

u_δ ovalization parameter

u_ε uniform convergence parameter

u_x horizontal ground displacements

$\tilde{u}_{xi}$ horizontal ground displacement measured at point i

u_y vertical ground displacements

$\tilde{u}_{yi}$ vertical ground displacement measured at point i

u_y^0 centerline surface settlement

U, V full space solution (horizontal and vertical displacements)

w_k branch points of $\phi(w)$

x distance from the tunnel centerline

$[x, y, z]$ Global coordinate system

$[x', y', z']$ Local coordinate system

y depth measured from the ground surface

z, z_k complex parameters

Greek

α dip angle of plane with isotropic properties

β_{ij} coefficients related to stiffness parameters

γ_{ij} shear strain

ΔV_s volume loss at the ground surface

$\Delta V_L/V_0$ volume loss at the tunnel cavity

ε_i normal strain

ζ_k transformed variable

θ angle

λ_k roots of the characteristic equation (with positive imaginary part)

ν Poisson's ratio (isotropic case)

ν_l Poisson's ratio for the effect of strains in the isotropic plane (x'-z')

ν_2	Poisson's ratio for the effect of strain in y' due to strain in the x' direction
ν_{hh}	Poisson's ratio for the effect of horizontal on complementary horizontal strain
ν_{hv}	Poisson's ratio for the effect of horizontal on vertical strain
ν_{vh}	Poisson's ratio for the effect of vertical strain on horizontal strain
ξ	integration variable
ρ	ovalization ratio
σ	analytic coefficient
σ_i	normal stress
σ_{v0}	overburden pressure
Σ_k	boundary in ζ_k domain
τ_{ij}	shear stress
$\Phi_k(z)$	analytic function

Superscripts

$+$	corresponding to cavity at $(0, H)$
$-$	corresponding to cavity at $(0, -H)$
c	"corrective" solutions

Subscripts

B	boundary
k	integer (assumes values 1, 2)

LIST OF FIGURES

LIST OF TABLES

β_{11}	$\cos^2\alpha\left(\dfrac{\cos^2\alpha}{E_1}-\dfrac{\nu_2\sin^2\alpha}{E_2}\right)+\sin^2\alpha\left(\dfrac{\sin^2\alpha}{E_2}-\dfrac{\nu_2\cos^2\alpha}{E_2}\right)-E_1\left(\dfrac{\nu_1\cos^2\alpha}{E_1}+\dfrac{\nu_2\sin^2\alpha}{E_2}\right)^2+\dfrac{\sin^2 2\alpha}{4G_2}$
β_{12}	$\sin^2\alpha\left(\dfrac{\cos^2\alpha}{E_1}-\dfrac{\nu_2\sin^2\alpha}{E_2}\right)-E_1\left(\dfrac{\nu_1\cos^2\alpha}{E_1}+\dfrac{\nu_2\sin^2\alpha}{E_2}\right)\left(\dfrac{\nu_1\sin^2\alpha}{E_1}+\dfrac{\nu_2\cos^2\alpha}{E_2}\right)+...$ $+\cos^2\alpha\left(\dfrac{\sin^2\alpha}{E_2}-\dfrac{\nu_2\cos^2\alpha}{E_2}\right)-\dfrac{\sin^2 2\alpha}{4G_2}$
β_{22}	$\sin^2\alpha\left(\dfrac{\sin^2\alpha}{E_1}-\dfrac{\nu_2\cos^2\alpha}{E_2}\right)+\cos^2\alpha\left(\dfrac{\cos^2\alpha}{E_2}-\dfrac{\nu_2\sin^2\alpha}{E_2}\right)-E_1\left(\dfrac{\nu_1\sin^2\alpha}{E_1}+\dfrac{\nu_2\cos^2\alpha}{E_2}\right)^2+\dfrac{\sin^2 2\alpha}{4G_2}$
β_{16}	$\sin 2\alpha\left(\dfrac{\sin^2\alpha-\nu_2\cos 2\alpha}{E_2}-\dfrac{\cos^2\alpha}{E_1}\right)+E_1\sin 2\alpha\left(\dfrac{\nu_1\cos^2\alpha}{E_1}+\dfrac{\nu_2\sin^2\alpha}{E_2}\right)\left(\dfrac{\nu_1}{E_1}-\dfrac{\nu_2}{E_2}\right)+\dfrac{\sin 4\alpha}{4G_2}$
β_{26}	$\sin 2\alpha\left(\dfrac{\cos^2\alpha+\nu_2\cos 2\alpha}{E_2}-\dfrac{\sin^2\alpha}{E_1}\right)+E_1\sin 2\alpha\left(\dfrac{\nu_1\sin^2\alpha}{E_1}+\dfrac{\nu_2\cos^2\alpha}{E_2}\right)\left(\dfrac{\nu_1}{E_1}-\dfrac{\nu_2}{E_2}\right)-\dfrac{\sin 4\alpha}{4G_2}$
β_{66}	$\sin^2 2\alpha\left(\dfrac{1}{E_1}+\dfrac{1+2\nu_2}{E_2}\right)-E_1\sin^2 2\alpha\left(\dfrac{\nu_1}{E_1}-\dfrac{\nu_2}{E_2}\right)^2+\dfrac{\cos^2 2\alpha}{G_2}$

Table 1: β coefficients used in analytical solution

1

tunnel face with support
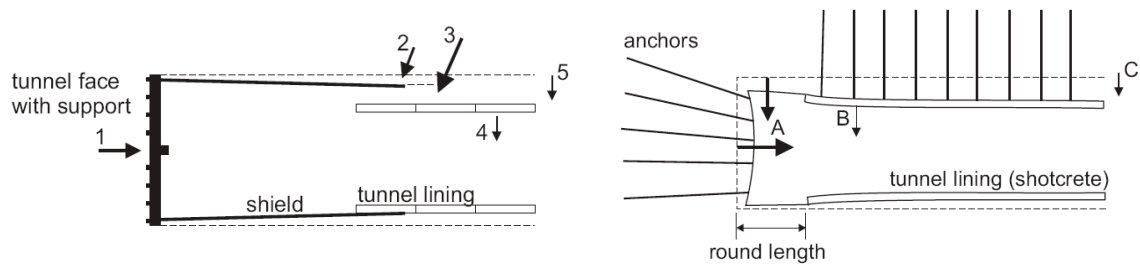
1. Stress relief at tunnel face
2. Shield over-cut & ploughing
3. Tail Void
4. Deformation of lining
5. Consolidation of soil

A. Deformation at tunnel heading
B. Deformation of lining
C. Consolidation of soil

a) Closed-face tunnel   b) Sequential excavation

Figure 1: Sources of ground movements associated with tunneling

(adapted from Möller, 2006)
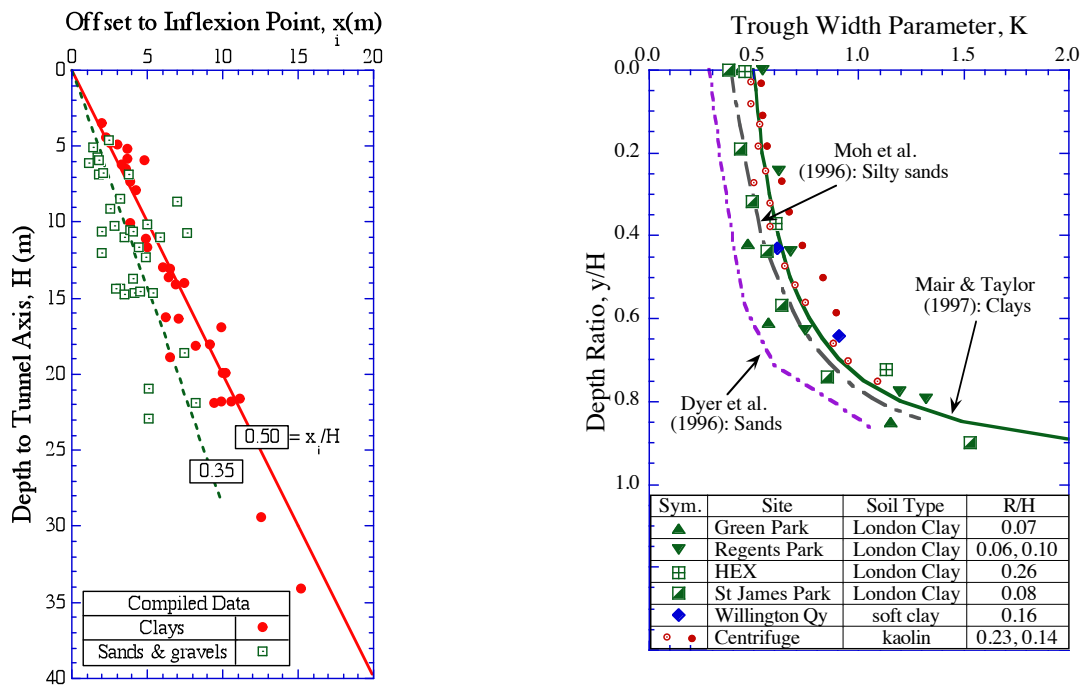
a) Width of surface settlement troughs   b) Width of sub-surface settlement troughs

Figure 2: Empirical estimation of inflexion point (after Mair & Taylor, 1997)

Figure3
Click here to download Figure: Figure03_updated.pdf

$$\frac{\Delta V_L}{V_0} = -\frac{2u_\varepsilon}{R}$$

Volume Loss: $\dfrac{\Delta V_L}{V_0} = -\dfrac{2u_\varepsilon}{R}$ Relative Distortion: $\rho = -\dfrac{u_\delta}{u_\varepsilon}$
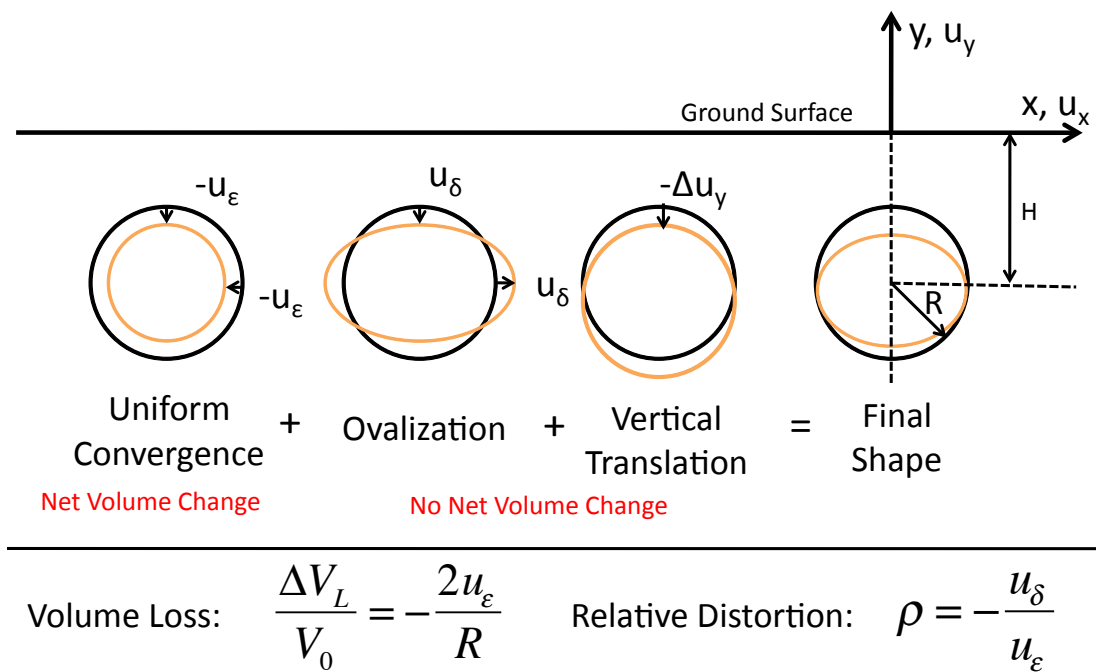
(Not to scale)

Figure 3: Deformation modes around tunnel cavity (after Whittle & Sagaseta, 2003)
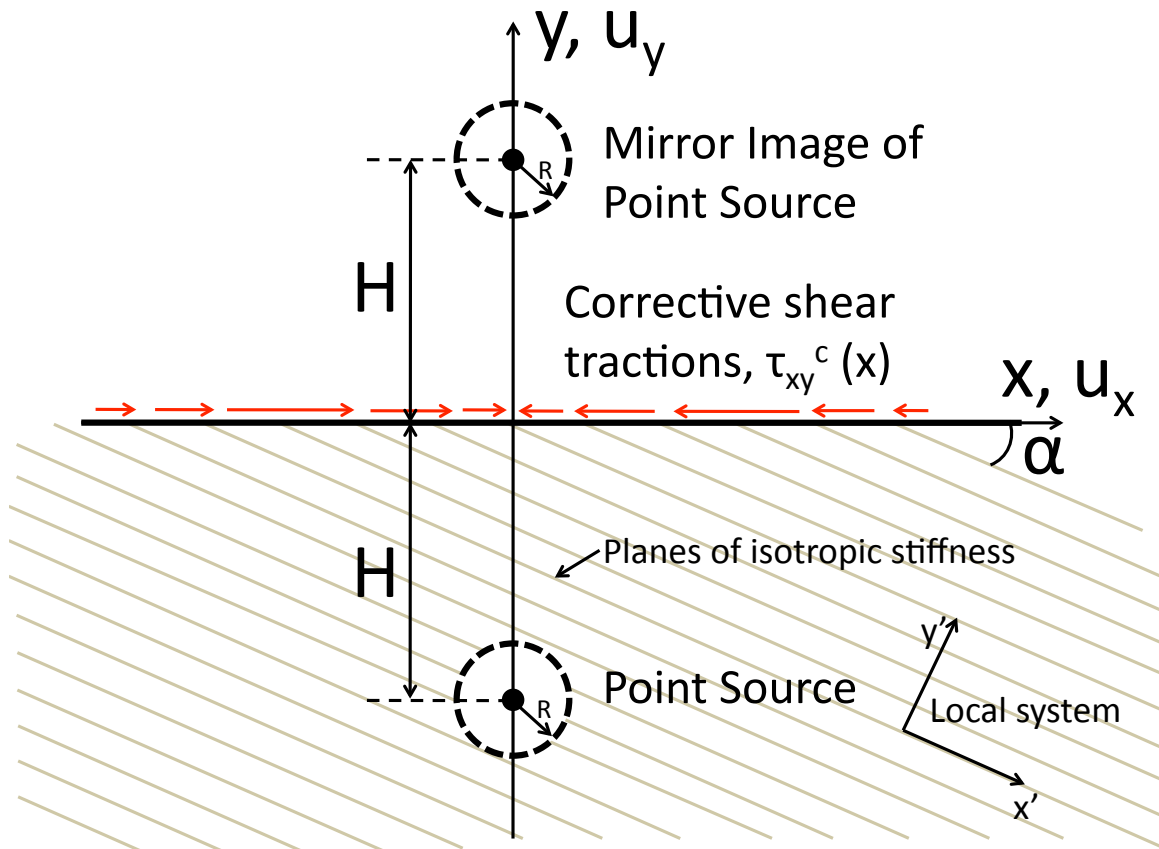
Figure 4: Superposition method to represent shallow tunnel in cross-anisotropic soil
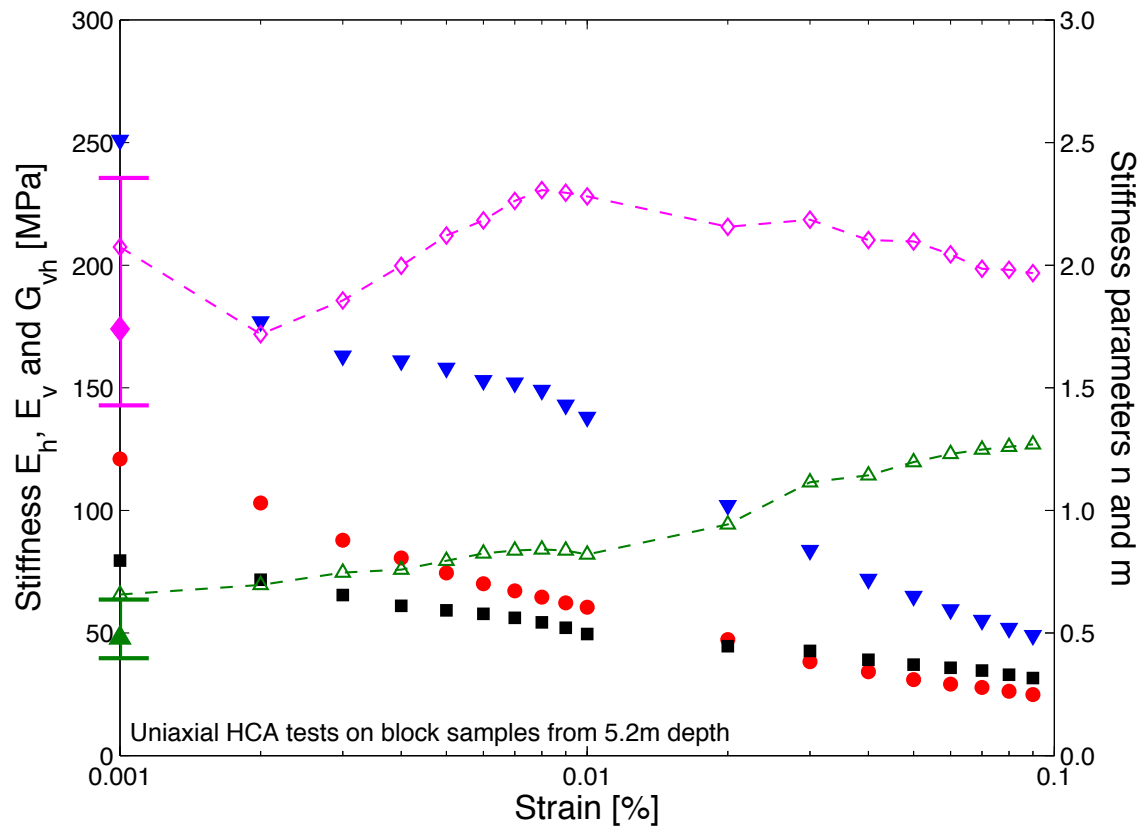
Figure 5: Anisotropic stiffness ratios from drained HCA uniaxial loading tests on natural London Clay (after Gasparre et al., 2007)
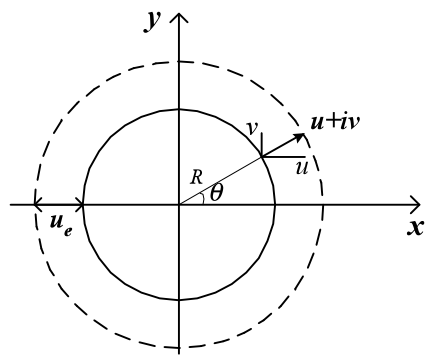
i) Uniform convergence
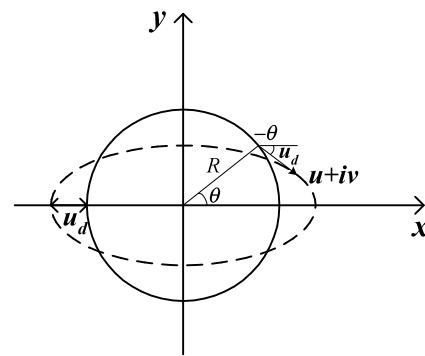
ii) Ovalization

Figure 6a: Prescribed displacement modes at tunnel cavity
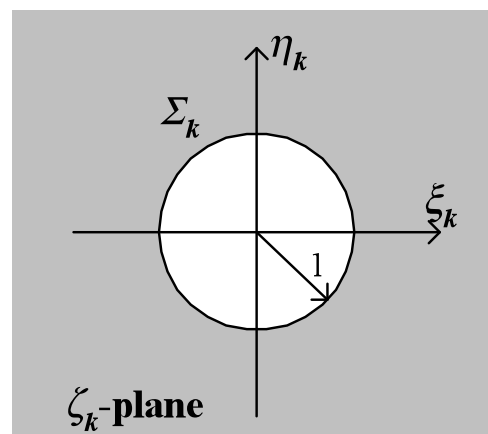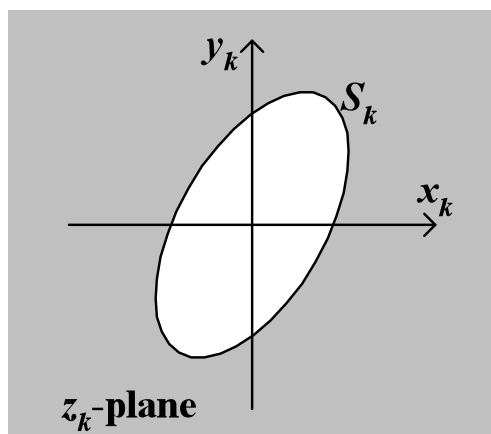
z_k-plane

ζ_k-plane

Figure 6b: Problem boundaries in z_k-plane and in transformed plane
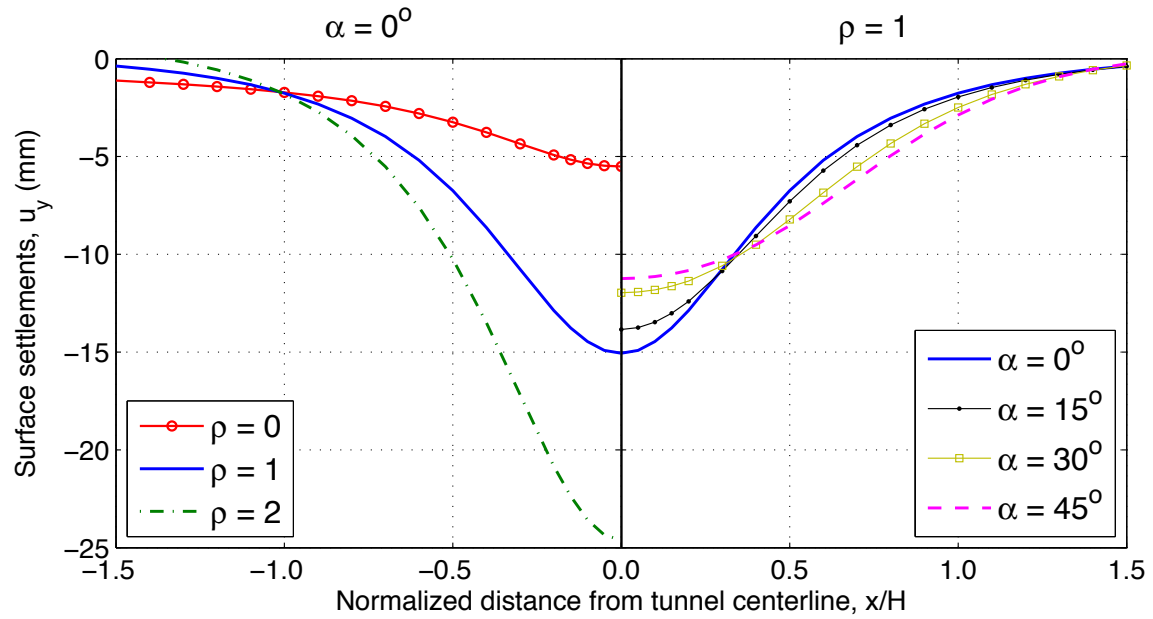
a) Surface Settlements
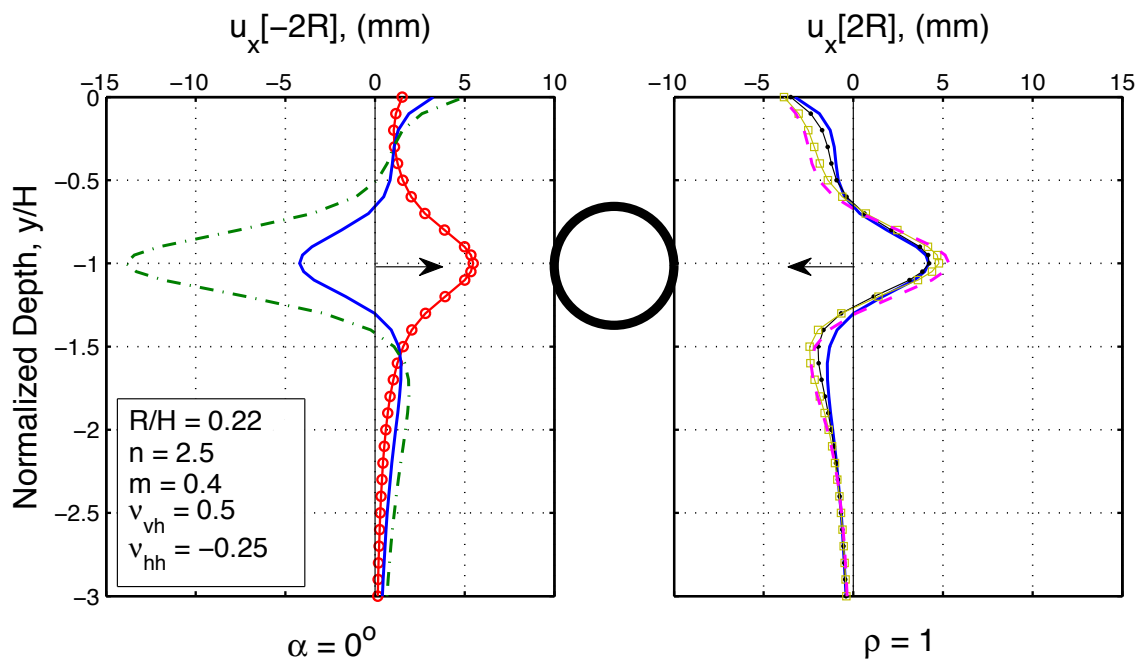
b) Lateral Displacements at x/2R = 1

Figure 7: Effect of relative distortion and dip angle on predicted surface settlements and subsurface lateral displacements for cross-anisotropic clay
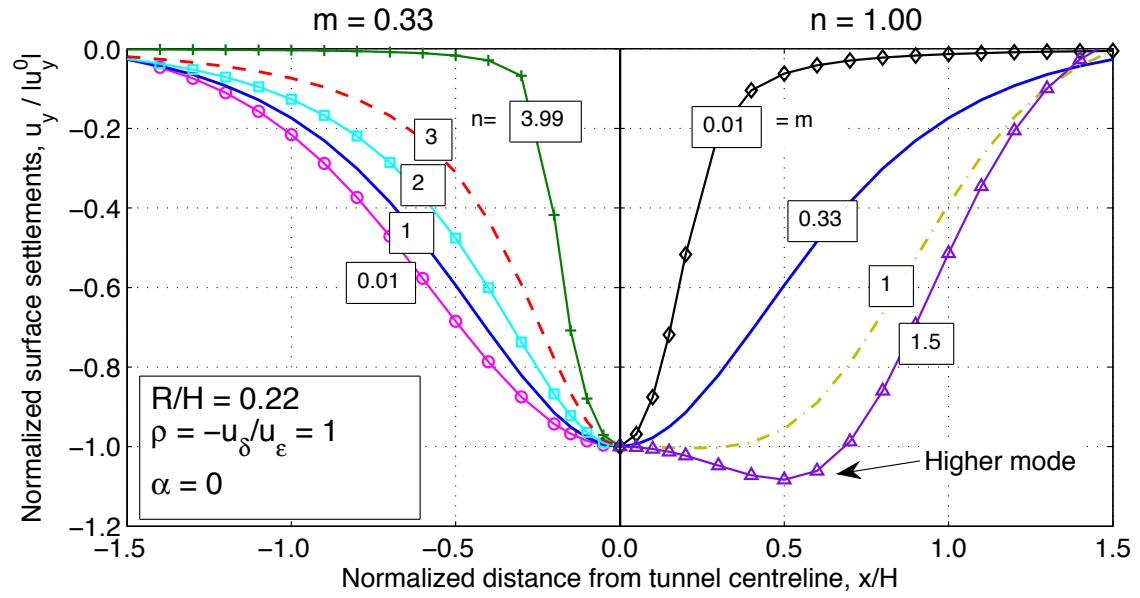
a) Normalized surface settlement trough
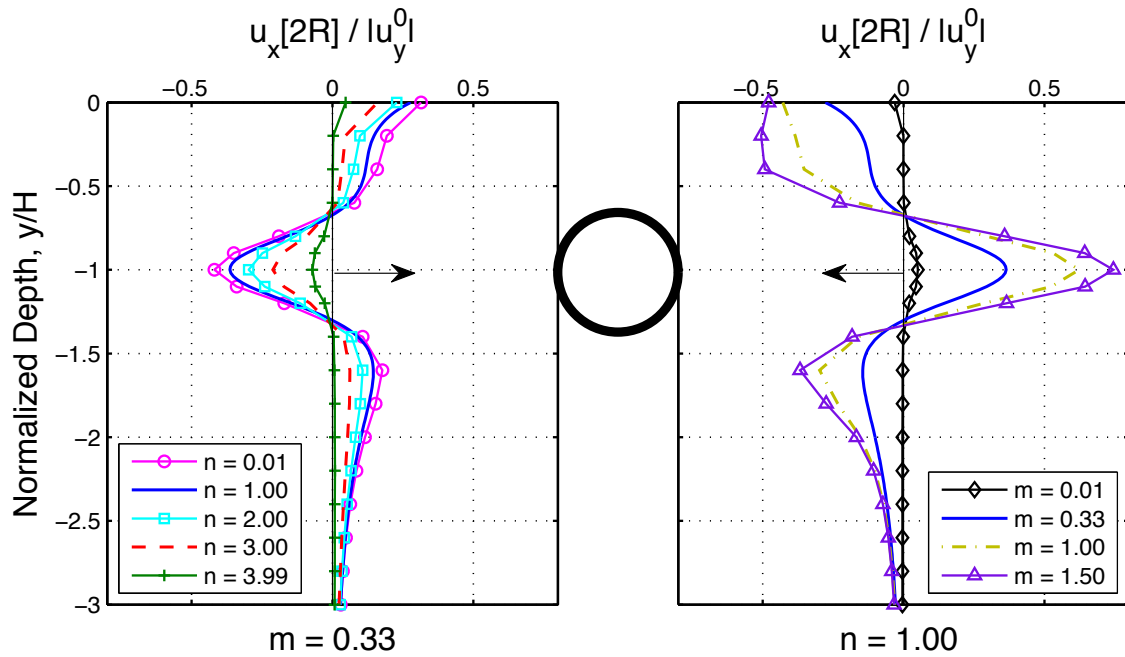
b) Normalized lateral displacements at offset, $x/2R = 1$

Figure 8: Effect of anisotropic stiffness ratios (n and m) on predicted surface settlements and subsurface lateral displacements
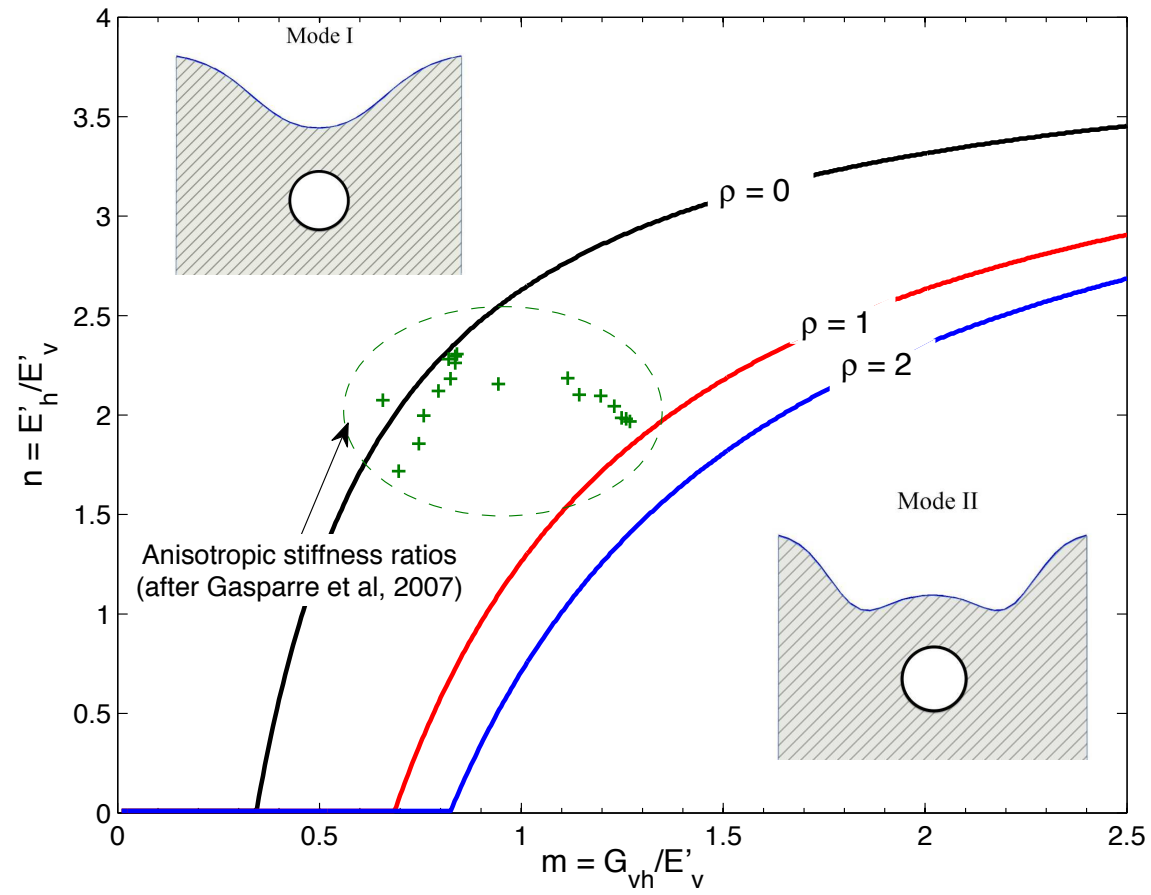
Figure 9: Effect of anisotropic stiffness ratios and tunnel ovalization ratio on the surface settlement trough mode shapes for shallow tunnels
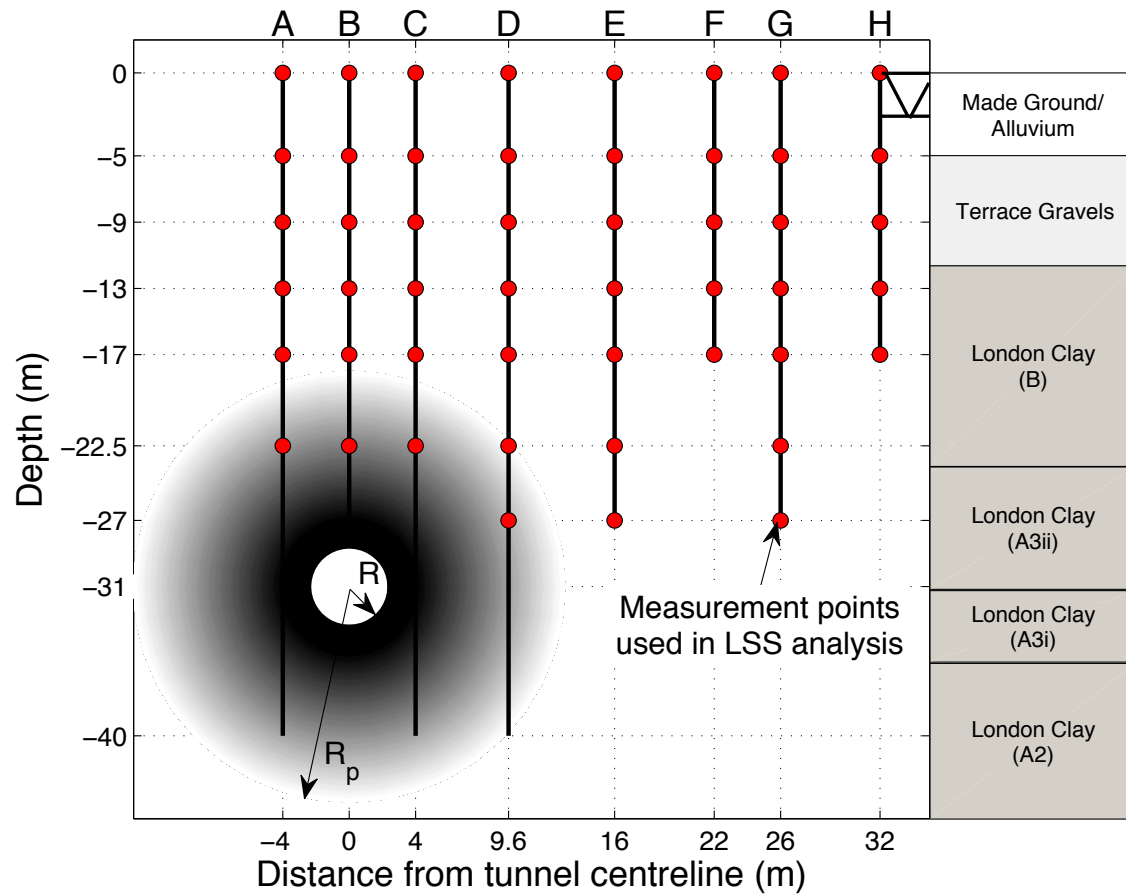
Figure 10: Cross-section and instrumentation of test section of JLE project in St James's Park – shading indicates plastic zone around tunnel (R_p/R=4-13)
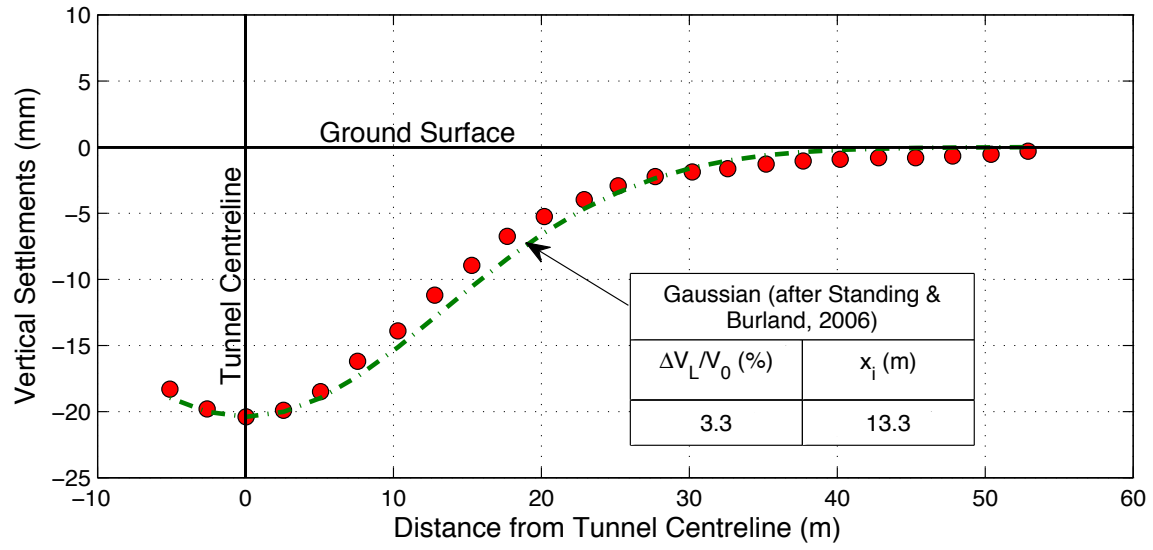
a) Surface settlement trough (after Standing & Burland, 2006)
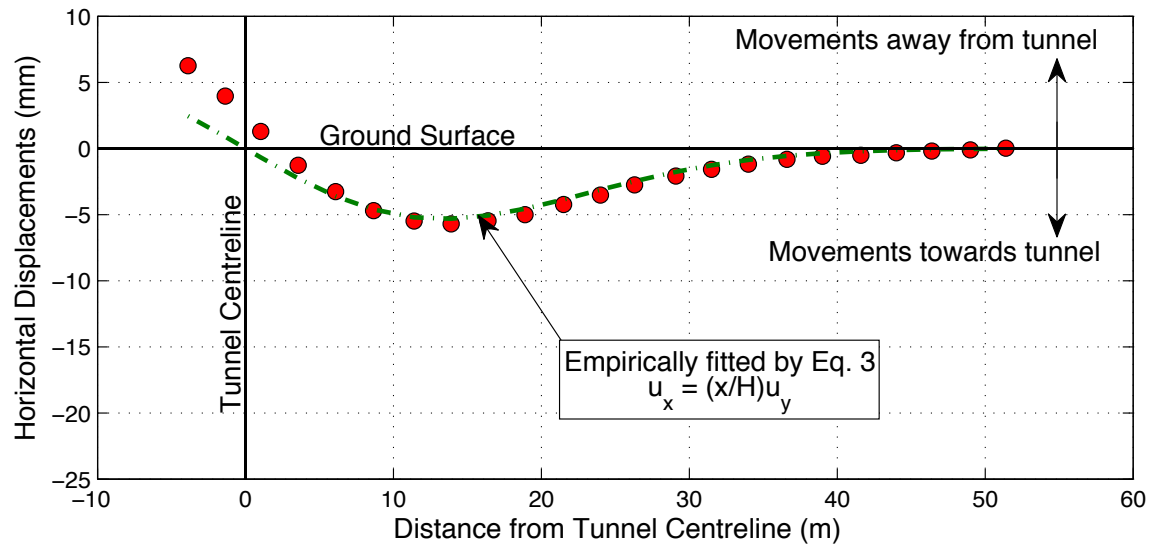
b) Surface horizontal displacements

Figure 11: Empirical interpretation of surface displacements for WB JLE tunnel in St.
James Park
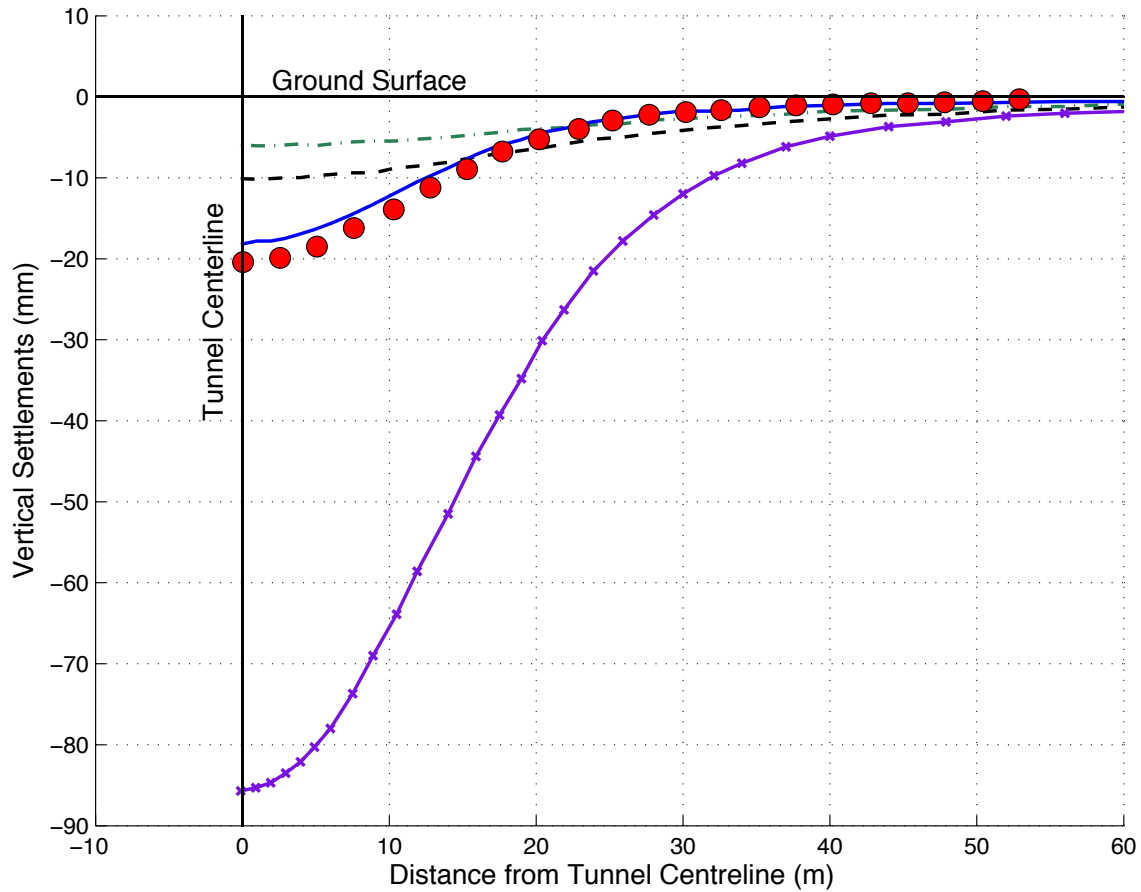
Line	Model	Dimensions	K_0	$\Delta V_L/V_0$ (%)	n	m
Finite Element analysis results, after Franzius et al. (2005)						
– – – –	Isotropic	2D	1.5	-3.3	1	0.55
– · – · –	Isotropic	3D	1.5	-2.1	1	0.55
———	Anisotropic	2D	0.5	-3.5	6.25	1.14
—×—	Anisotropic	3D	0.5	-18.1	6.25	1.14
●	Field Measurements					

Figure 12: Surface settlement troughs as predicted by FE analysis undertaken by Franzius et al (2005)
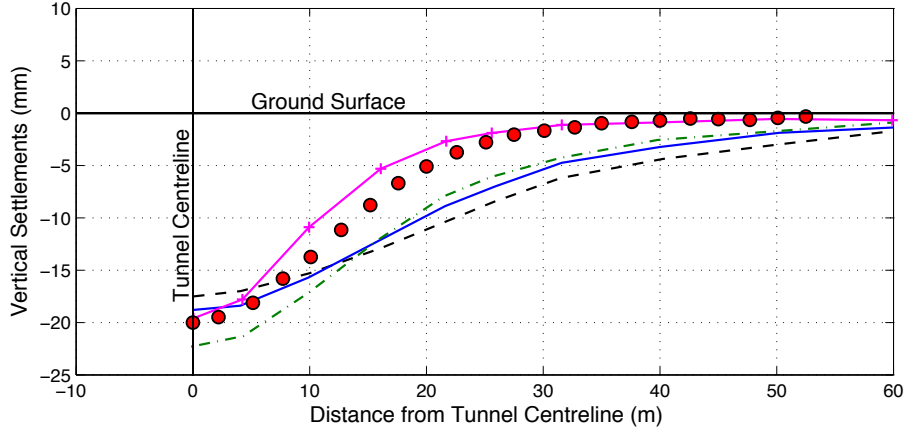
a) Surface settlement trough

b) Subsurface Lateral Displacements
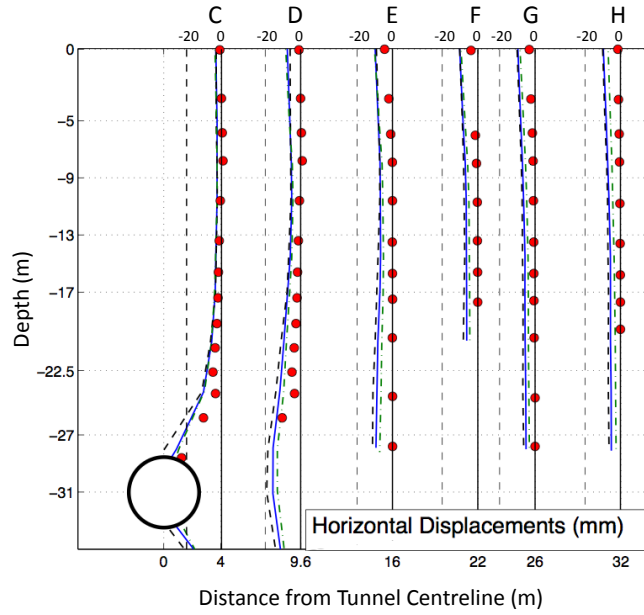
Line	Model	K_0	G_{hh}/G_{vh}	$\Delta V_L/V_0$ (%)	n	m
3D Finite Element analysis results, after Wongsaroj (2005)						
– – –	Isotropic	1.5	1.0	6.0	1.000	0.435
——	Anisotropic	1.5	1.5	5.6	0.438	0.130
–·–·–	Anisotropic	1.0	1.5	5.4	0.438	0.130
—+—	Anisotropic	1.2	5.0	3.2	0.438	0.039
●	Field Measurements				$\left(n=\dfrac{v'_{vh}}{v'_{hv}}\right)$	$\left(m=\dfrac{n}{2(1+v'_{hh})}\cdot\dfrac{G_{vh}}{G_{hh}}\right)$
Poisson's Ratios: Isotropic ($v'_{vh}=v'_{hh}=v'_{hv}=0.15$); Anisotropic Model ($v'_{vh}=0.07$, $v'_{hh}=0.12$, $v'_{hv}=0.16$)						

Figure 13: Comparison between field measurements and FE analysis results undertaken by Wongsaroj (2005)
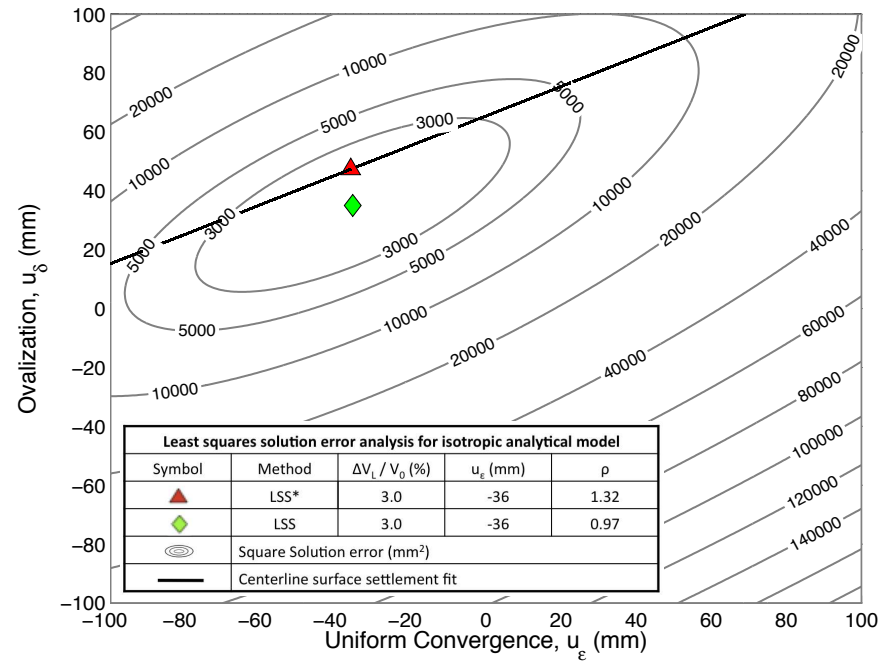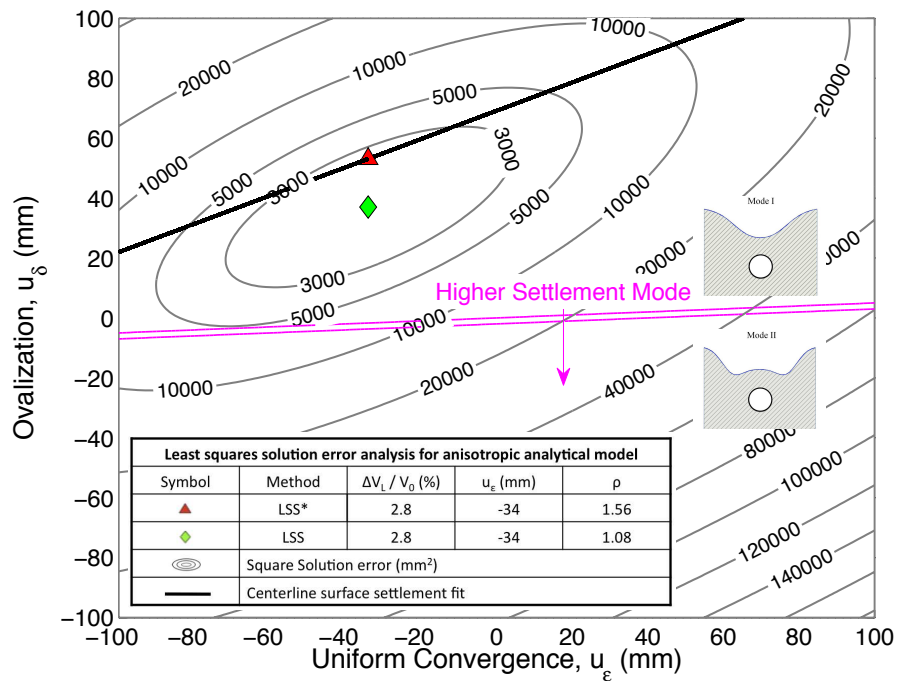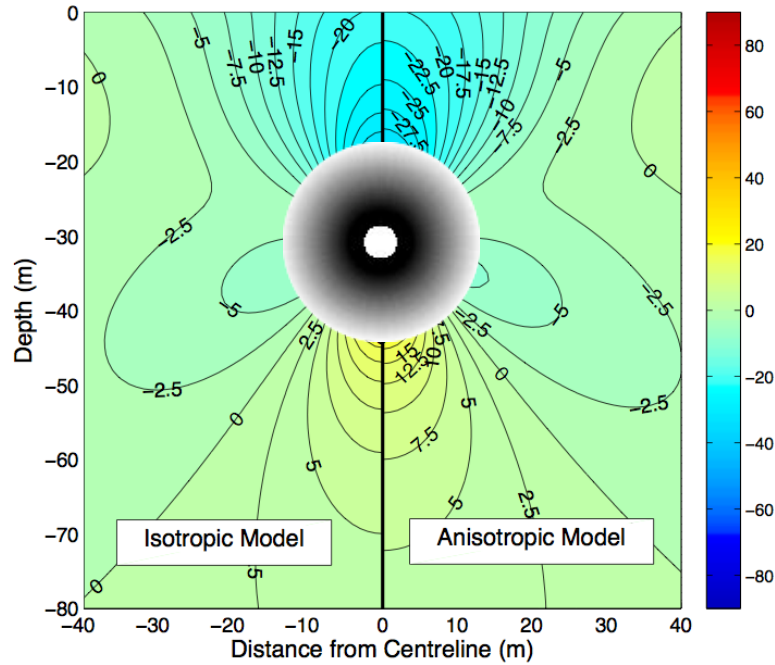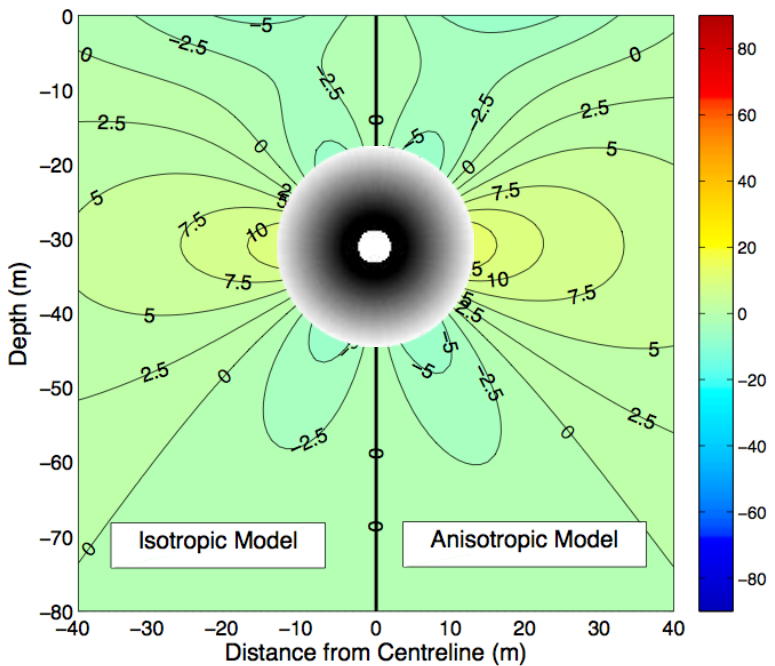
a) Isotropic case

b) Cross-anisotropic case

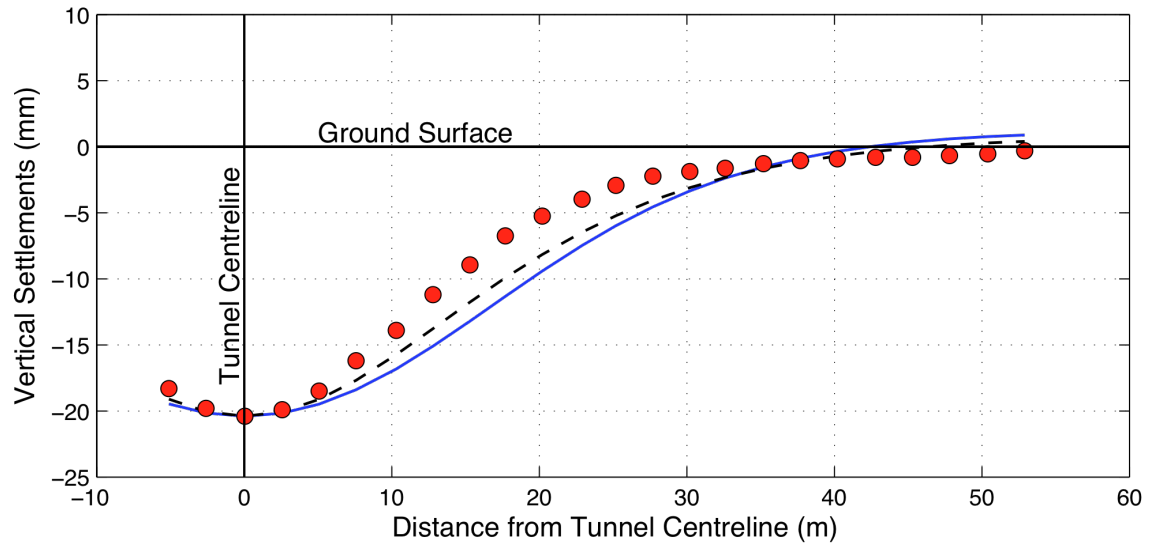Figure 14: Least squares error analysis undertaken for input parameter selection
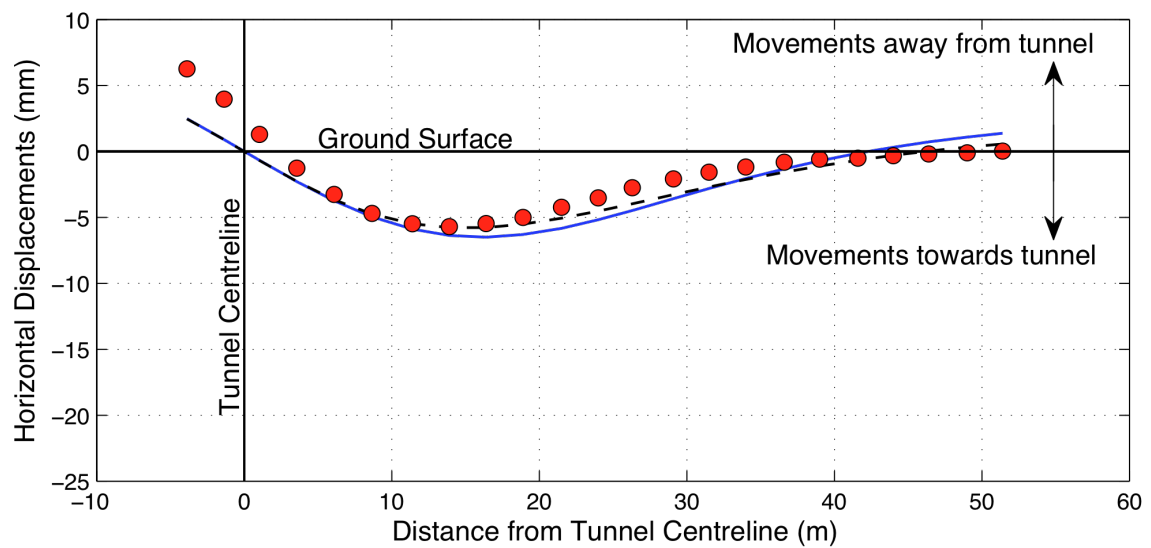
a) Vertical displacements (mm)

b) Horizontal displacements (mm)

Figure 15: Analytical predictions of vertical and horizontal ground deformations for LSS* solutions with isotropic and cross-anisotropic stiffness properties for London Clay
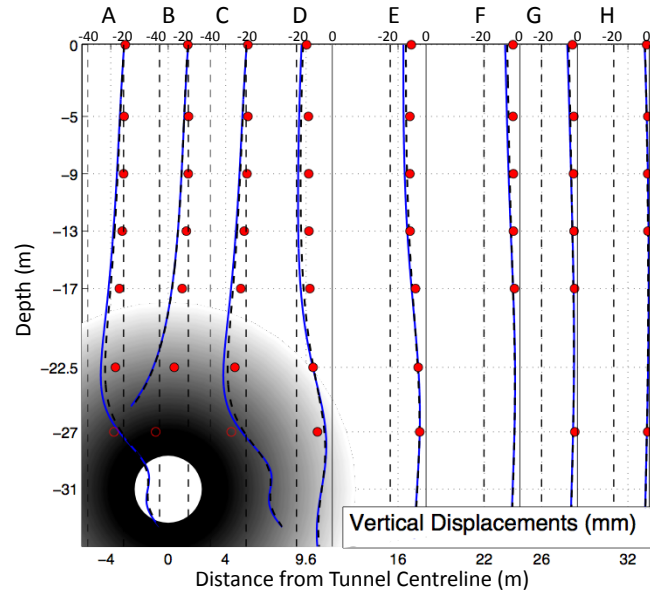
Figure16
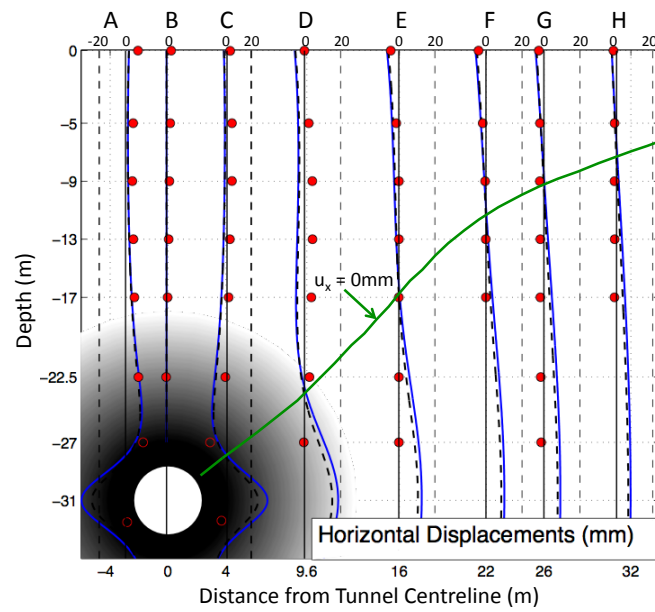Click here to download Figure: Figure16.pdf

a) Settlements

b) Horizontal displacements

Line	Analytical Model	u_ε (mm)	$\Delta V_L/V_0$ (%)	ρ
– – –	Isotropic	-36.0	3.0	1.32
——	Anisotropic	-34.0	2.8	1.56
●	Field Measurements			

Figure 16: Comparison of computed and measured surface movements for WB JLE tunnel

a) Vertical Displacements

b) Horizontal displacements

Line	Analytical Model	u_ε (mm)	$\Delta V_L/V_0$ (%)	ρ
– – – –	Isotropic	-36.0	3.0	1.32
——	Anisotropic	-34.0	2.8	1.56
●	Field Measurements			

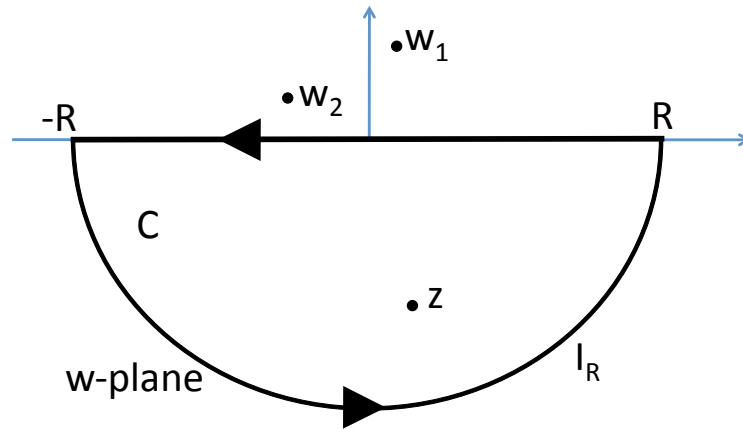Figure 17: Comparison of computed and measured subsurface ground movements for WB JLE tunnel

Figure B1: Integration path